University of Groningen

A GBT Survey of the HALOGAS Galaxies and Their Environments. I. Revealing the Full Extent of HI around NGC 891, NGC 925, NGC 4414, and NGC 4565

Pingel, N. M.; Pisano, D. J.; Heald, G.; Jarrett, T. H.; de Blok, W. J. G.; Jozsa, G. I. G.; Juette, E.; Rand, R. J.; Oosterloo, T.; Winkel, B.

Published in:
Astrophysical Journal

DOI:
10.3847/1538-4357/aad816

IMPORTANT NOTE: You are advised to consult the publisher's version (publisher's PDF) if you wish to cite from it. Please check the document version below.

Document Version
Publisher's PDF, also known as Version of record

Publication date:
2018

Link to publication in University of Groningen/UMCG research database

Citation for published version (APA):
Pingel, N. M., Pisano, D. J., Heald, G., Jarrett, T. H., de Blok, W. J. G., Jozsa, G. I. G., Juette, E., Rand, R. J., Oosterloo, T., & Winkel, B. (2018). A GBT Survey of the HALOGAS Galaxies and Their Environments. I. Revealing the Full Extent of HI around NGC 891, NGC 925, NGC 4414, and NGC 4565. *Astrophysical Journal*, *865*(1), [36]. https://doi.org/10.3847/1538-4357/aad816

Copyright
Other than for strictly personal use, it is not permitted to download or to forward/distribute the text or part of it without the consent of the author(s) and/or copyright holder(s), unless the work is under an open content license (like Creative Commons).

The publication may also be distributed here under the terms of Article 25fa of the Dutch Copyright Act, indicated by the “Taverne” license. More information can be found on the University of Groningen website: https://www.rug.nl/library/open-access/self-archiving-pure/taverne-amendment.

Take-down policy
If you believe that this document breaches copyright please contact us providing details, and we will remove access to the work immediately and investigate your claim.

Downloaded from the University of Groningen/UMCG research database (Pure): http://www.rug.nl/research/portal. For technical reasons the number of authors shown on this cover page is limited to 10 maximum.

The Astrophysical Journal, 865:36 (27pp), 2018 September 20 https://doi.org/10.3847/1538-4357/aad816

A GBT Survey of the HALOGAS Galaxies and Their Environments. I. Revealing the Full Extent of H I around NGC 891, NGC 925, NGC 4414, and NGC 4565

N. M. Pingel[1,2], D. J. Pisano[1,2,3], G. Heald[4,5], T. H. Jarrett[6], W. J. G. de Blok[5,6,7], G. I. G. Józsa[8,9,10], E. Jütte[11], R. J. Rand[12], T. Oosterloo[5,7], and B. Winkel[13]
[1] Department of Physics and Astronomy, West Virginia University, White Hall, Box 6315, Morgantown, WV 26506, USA; nipingel@mix.wvu.edu
[2] Center for Gravitational Waves and Cosmology, West Virginia University, Chestnut Ridge Research Building, Morgantown, WV 26505, USA
[3] Adjunct Astronomer at Green Bank Observatory, P.O. Box 2, Green Bank, WV 24944, USA
[4] CSIRO Astronomy and Space Science, P.O. Box 1130, Bentley, WA 6102, Australia
[5] Netherlands Institute for Radio Astronomy (ASTRON), Postbus 2, 7990 AA Dwingeloo, The Netherlands
[6] Department of Astronomy, University of Cape Town, Private Bag X3, Rondebosch 7701, South Africa
[7] Kapteyn Astronomical Institute, University of Groningen, P.O. Box 800, 9700 AV, Groningen, The Netherlands
[8] South African Radio Astronomy Observatory (SARAO), SKA South Africa, The Park, Park Road, Pinelands, 7405, South Africa
[9] Rhodes University, Radio Astronomy Research Group (RARG), P.O. Box 94, Grahamstown, 6140, South Africa
[10] Argelander-Institut für Astronomie, Auf dem Hügel 71, D-53121 Bonn, Germany
[11] Astronomisches Institut Ruhr-Universität Bochum, Universitätsstraße 150, D-44780 Bochum, Germany
[12] Department of Physics and Astronomy, University of New Mexico, Albuquerque, NM 87131, USA
[13] Max-Planck-Institut für Radioastronomie (MPIfR), Auf dem Hügel 69, D-53121, Germany

Received 2017 April 3; revised 2018 August 2; accepted 2018 August 3; published 2018 September 18

Abstract

We present initial results from a deep neutral hydrogen (H I) survey of the HALOGAS galaxy sample, which includes the spiral galaxies NGC 891, NGC 925, NGC 4414, and NGC 4565, performed with the Robert C. Byrd Green Bank Telescope (GBT). The resulting observations cover at least 4 deg^2 around these galaxies, with an average 5σ detection limit of 1.2×10^{18} cm^{-2} over a velocity range of 20 km s^{-1} and angular scale of $9\overset{\prime}{.}1$. In addition to detecting the same total flux as the GBT data, the spatial distribution of the GBT and original Westerbork Synthesis Radio Telescope data match well at equal spatial resolutions. The H I mass fraction below H I column densities of 10^{19} cm^{-2} is, on average, 2%. We discuss the possible origins of low column density H I of nearby spiral galaxies. The absence of a considerable amount of newly detected H I by the GBT indicates these galaxies do not have significant extended diffuse H I structures, and suggests future surveys planned with the SKA and its precursors must go *at least* as deep as 10^{17} cm^{-2} in column density to significantly increase the probability of detecting H I associated with the cosmic web and/or cold mode accretion.

Key words: galaxies: evolution – galaxies: formation – galaxies: individual (NGC 891, NGC 925, NGC 4414, NGC 4565)

1. Introduction

Resolved neutral hydrogen (H I) observations undertaken over the past decade have revealed many intricate details related to the morphology and dynamics of spiral galaxies. A primary science goal of recent large surveys is to develop a deep understanding of how physical processes within the disks of spiral galaxies, such as star formation and the subsequent stellar feedback, affect their local circumgalactic environments. Surveys such as The H I Nearby Galaxy Survey (THINGS; Walter et al. 2008) and Hydrogen Accretion in LOcal GAlaxies Survey (HALOGAS; Heald et al. 2011; hereby referred to as H11) performed with the Very Large Array (VLA) and Westerbork Synthesis Radio Telescope (WSRT), respectively, provide high-resolution maps of the environments around nearby spiral galaxies.

Accretion of diffuse gas onto the disks of galaxies from the intergalactic medium (IGM) is a possible explanation for how the H I content of galaxies has remained relatively constant since $z \sim 2$ while the star formation rate (SFR) was up to 10 times higher at high redshifts (Noterdaeme et al. 2012; Madau & Dickinson 2014). The constant H I content implies that galaxies have somehow replenished themselves with enough gas to fuel continuous star formation. And though not directly responsible for star formation, H I is an intermediate phase toward molecular hydrogen, which is the raw ingredient of the star formation fuel. If the star formation is to continue, external gas has to be accreted and pass through the H I phase at some stage in the accretion process. Observationally inferred accretion rates as traced by H I, however, fall between 0.1 and 0.2 $M_{\odot}$ at low redshifts. This is a full order of magnitude lower than what is needed for galaxies to continually form stars at their current rates (Sancisi et al. 2008; Kauffmann et al. 2010). This discrepancy presents two intriguing scenarios: the cycle of star formation will eventually exhaust all of the available fuel within a few Gyr and star formation itself will gradually cease, or processes that refuel galaxies with the necessary gas have been missed by previous surveys. Numerical simulations have shown a likely mechanism for refueling star formation is through a quasi-spherical "hot" mode and filamentary "cold" mode (Birnboim & Dekel 2003; Kereš et al. 2005, 2009). "Cold" in the context of these numerical simulations refers to gas that has not been heated above the virial temperature of the galaxy's potential well ($\sim 10^5$ K), and "hot" refers to gas that has virialized in a process akin to the classical theory of galaxy formation in which shock-heated, virialized gas with short cooling timescales accretes onto the central galaxy (e.g., Rees & Ostriker 1977). These simulations also suggest cold mode accretion was the dominant form of accretion at $z \geqslant 1$ for all systems, and remains prevalent through $z = 0$ for galaxies in low-density environments ($n_{\mathrm{gal}} \lesssim 1\ \mathrm{h}^3\ \mathrm{Mpc}^{-3}$) and $M_{\mathrm{halo}} \lesssim 10^{11.4}\ M_{\odot}$ (or $M_{\mathrm{bary}} \leqslant 10^{10.3}\ M_{\odot}$). For perspective, our own Milky Way has a virial (and thus halo) mass on the order of $10^{12}\,M_\odot$. These cold flows should exist in the form of vast filaments of cold, diffuse gas that permeate through the hot halo (Kereš et al. 2005). Comparisons by Nelson et al. (2013) between the smoothed particle hydrodynamic (SPH) numerical scheme employed in Kereš et al. (2005, 2009) and more sophisticated adaptive mesh refinement (AMR) simulations revealed the relative contribution of the cold mode is likely overestimated in earlier SPH simulations due to inherent numerical deficiencies. Nevertheless, the AMR simulations do show *some* fraction of gas is accreted cold.

The temperature of the gas in these predicted cold filaments is too high for a significant amount of neutral gas to exist within the largely ionized medium. However, AMR hydrodynamic simulations presented by Joung et al. (2012) show large amplitude nonlinear perturbations can create cooling instabilities in which gas is collisionally excited and cools through subsequent radiative de-excitation of excited states. Large filamentary flows of inflowing gas are a possible seeding mechanism for nonlinear perturbations, which allow gas to cool enough to form H I clouds within the innermost regions of the halo ($R \leqslant 100$ kpc) at H I column densities ($N_{\rm H\,I} \leqslant 10^{18}$ cm^{-2}) currently detectable with existing telescopes.

More recent independent ballistic models show galactic fountain activity can account for the presence of extraplanar H I around the Milky Way (in clouds like Complex C; Fraternali et al. 2015) and NGC 891 (Fraternali & Binney 2006). In addition, Fraternali (2017) describes the condensation of hot coronal gas in the wake of the interaction with cooler galactic fountain gas, showing that fountain driven accretion can cool enough lower coronal gas to sufficiently extend the gas depletion time.

Observational evidence for predicted cold flows is very limited. Through absorption measurements, Stocke et al. (2010) and Ribaudo et al. (2011) both find low-metallicity gas infalling onto a nearby solar metallicity Lymann Limit System whose mass is consistent with the presence of cold flows predicted by simulations. The presence of infalling, low-metallicity gas is certainly consistent with cold flows, but these measurements do not reveal any information about the extended spatial distribution of the accretion. Absorption measurements are very promising in that they accurately probe the metallicity of galaxy halos, but such studies require a quasar or other bright background source to measure the absorption line of interest. Absorption studies of the Milky Way, in which these desired sightlines are abundant, show our own Galaxy is surrounded by an immense amount of low column density gas that is both ionized and neutral (e.g., Wakker et al. 2003; Richter et al. 2017), with temperatures ranging from 10^2 to 10^7 K. Detection in emission does not rely on serendipitous sightlines required for external galaxies, and will constrain the large-scale extent of the predicted cold flows or a potential diffuse component.

The unrivaled point source response of radio interferometers like the WSRT and VLA allows for incredible high-resolution mapping capabilities at angular resolutions $\sim\frac{\lambda}{b_{\rm max}}$, where $b_{\rm max}$ is the maximum baseline ($b_{\rm max} = 2.7$ km for the WSRT), which reveals the small scale structure of galaxies. On the downside, interferometers act as spatial filters by construction, and in particular due to the minimum possible spacing between neighboring telescopes in an interferometer (i.e., the physical size of each dish), there is a gap in $u - v$ coverage at large angular scales from the absence of short baselines. This gap is often referred to as the "short-spacing" problem, and it limits the amount of large-scale structure an interferometer is able to detect (e.g., Braun & Walterbos 1985). As a consequence of the lack of sensitivity at large angular scales, past H I observations performed with interferometers may have missed significant reservoirs of gas around galaxies. On the other hand, the H I is observed in channels covering small velocity ranges only, and thus potentially does not extend enough to cause the sampled baselines to miss several interesting low-density, diffuse features. The full $u - v$ coverage capability of single-dish telescopes (Stanimirovic 2002) permits the detection of structure at all angular scales to test that notion. The unblocked aperture design of the GBT and resulting low sidelobes coupled with the compromise between resolution ($9\rlap{.}'1$) and high surface brightness sensitivity ($T_{\rm sys} \lesssim 20$ K) make it the ideal instrument to look for low column density structure around the HALOGAS sources.

The few surveys that have mapped down to $N_{\rm H\,I} \lesssim 10^{19}$ cm^{-2} have uncovered several interesting low-density, diffuse features. Perhaps most notably, Braun & Thilker (2004) discovered a low column density H I filament connecting M31 and M33. Two possible explanations for its origin have been presented since its discovery: either it is similar to filaments seen in simulations of the cosmic web (Popping et al. 2009), and thus an observational example of the cold mode accretion process, or it was created via a past tidal interaction between M31 and M33 (Bekki 2008; Putman et al. 2009). Higher resolution observations with the GBT by Wolfe et al. (2013, 2016) show that this filament is clumpy in nature and made up of small H I clouds with $M_{\rm H\,I} \sim 10^{4-5}\,M_\odot$, $N_{\rm H\,I} \sim 10^{18}$ cm^{-2}, and diameters on the order of kpc. M31 has a $M_{\rm dyn} \sim 1.3 \times 10^{12}\,M_\odot$ (Corbelli et al. 2010), which suggests the cold mode accretion scenario is unlikely. Furthermore, the total H I mass of these clouds is only $4.6 \times 10^6\,M_\odot$, providing only meager neutral mass accretion rates for conservative infall time estimates of 10^{7-8} years. The origin of these clouds is still an open and intriguing question, which can be answered by utilizing sensitive observations of the H I within the circumgalactic environment of M31 and M33 (Wolfe et al. 2016).

Other recent detections by the GBT of large H I structures in NGC 6946 by Pisano (2014) and NGC 2403 by de Blok et al. (2014) suggest these features are seen around a variety of galaxies. In order to determine the true origin of these filaments, resolve the discrepancy between observed accretion rates and SFRs, and obtain a comprehensive understanding of how the disks of galaxies interact with their surrounding circumgalactic environment, a comprehensive H I census spanning a wide range of astrophysically interesting properties (e.g., dynamical mass, total H I mass, halo mass, SFRs, etc.) is required. A complete census of these properties will build up large number statistics and uncover any underlying correlations between intrinsic galaxy properties and possible signatures of accretion. The HALOGAS observations of 24 nearby galaxies obtained with the WSRT and the THINGS survey with the VLA are critical steps toward just such a census. To ensure this census is absolutely complete, interferometer observations must be supplemented with large single-dish observations to cover all angular scales to ensure large-scale emission is not resolved out by interferometers, and to map down to the lowest possible column density levels.

In this pilot paper, we present data and analysis from four sources from the HALOGAS survey: NGC 891, NGC 925, NGC 4414, and NGC 4565. These GBT maps are among the deepest ($N_{\rm H\,I} \sim 10^{18}$ cm^{-2}) for external galaxies obtained to date in H I. This paper serves as an introduction to the full survey as a way to outline our analysis methods and highlight our overall goals. In Section 2 we present an overview of the HALOGAS sample; the observing configuration, reduction strategy, and a discussion on our GBT beam model and how we convolve the WSRT data to avoid contamination from extended structure are outlined in Section 3. The results from our comparison between the GBT and WSRT data for our initial four sources are discussed in Section 4, with an investigation into how the diffuse H I environment relate to intrinsic galaxy properties following in Section 5. We then summarize our conclusions and comment on future work in Section 6.

2. The HALOGAS Data and Sample

2.1. WSRT Data Cubes

The high-resolution HALOGAS cubes were produced from data obtained with the WSRT. See H11 for complete details on the observational configuration and data reduction of these data; see also Oosterloo et al. (2007) for configuration and reduction details specific to NGC 891. A particular aspect of the HALOGAS observational setup we wish to highlight here is the minimum baseline length of 36 m, which translates to a maximum recoverable angular scale of ∼20′. As mentioned in the introduction, this particular angular scale is important because smooth emission extending above this limit will not be present in the WSRT data but fully observable by the GBT.

As will be discussed later, a significant portion of our analysis relies on convolved WSRT data convolved to the GBT resolution. Flux measurements from convolved data have the potential to be misleading, as convolved emission will extend outside the original “clean” boundaries used to produce the final interferometer cubes. Fully cleaned maps of array data are the sum of the restored clean components and residual map. Generally, only a portion of a map is cleaned, and thus will have the correct flux. The flux in uncleaned portions of the map will be overestimated by a factor equal to the ratio of the dirty beam size to clean beam size. We measure outside of the clean region because the convolution obviously extends source emission beyond its original boundaries. Including regions of uncleaned emission in the convolution will inevitably lead to misleading total flux measurements, as pixels with uncleaned emission have an intensity scale defined as Jy per dirty beam as opposed to Jy per clean beam (e.g., Jorsater & van Moorsel 1995). In the interest of quantifying how the inclusion of unclean emission will affect the overall flux measurements in the convolved WSRT data, we extract two sub-maps from the original WSRT high-resolution NGC 891 cubes that include a different number of pixels that were excluded from the cleaning as part of the data reduction. We then compare the total H I flux values after convolving these sub-maps as described in Section 3.2. Specifically, ∼60% of the first extracted subregion includes pixels that were part of the original clean region, while the remaining 40% of the pixels in this sub-map were excluded from the cleaning algorithm. In the second sub-map, ∼90% of the pixels were cleaned during data reduction, while the remaining 10% of the pixels were excluded from cleaning. We find the total flux measurements of these two sub-maps to be the same. This indicates that while some uncleaned emission—whether from pixels not inside the original clean region or simply low-level emission below the original clean threshold—is inevitably included, the total flux estimates are not significantly affected. That said, there are still systematic calibration uncertainties introduced by the specific treatment of the raw $u - v$ visibilities to consider. A few examples are the removal of residual baseline structure, flagged/missing baselines, antenna shadowing, and different weighting schemes applied to the complex visibilities. We adopt an overall systematic flux uncertainty of 5% to encapsulate uncertainties related to how the WSRT data were processed.

2.2. Sample

The total HALOGAS sample consists of 24 unbarred and barred, nearby spirals that span a very diverse range of astrophysically significant properties such as SFRs, H I mass ($M_{\rm H\,I}$), stellar mass (M_*), baryonic mass ($M_{\rm bary}$), and so on. The sample also consists of galaxies with a wide range of environments.

We adopt the best distance values listed for each source in H11. Given that the “best” distances were determined by taking the median measurements from well-established methods (e.g., Cepheid and/or tip of the red giant branch, planetary-nebulae luminosity function, Tully-Fisher distances), we adopt a conservative 10% overall uncertainty for these distances. The SFRs for all galaxies mentioned in this work besides NGC 4565 and NGC 2997 (to be discussed in Section 5.2 in regard to similar GBT data of nearby galaxies) are computed utilizing data from the 22 μm band of the *Wide-field Infrared Survey Explorer* (*WISE*), a space-based observatory deployed to map the entire sky in the infrared, along with far-ultraviolet (FUV) luminosity data from the *Galaxy Evolution Explorer* (*GALEX*; Gil de Paz et al. 2007). We follow the method outlined in Jarrett et al. (2013) to obtain an infrared SFR (SFR$_{\rm IR}$) that traces star formation obscured by dust, with further calibrations derived by Cluver et al. (2014) for the same IR bands. Due to the difficulty of disentangling the relative contribution from young and old stellar populations to various polycyclic aromatic hydrocarbon emission bands near 12 μm, we chose to use the SFR$_{\rm IR}$ derived from the *WISE* 22 μm band. The SFR tracing UV photons associated with young massive stars is given as

$$\log_{10}\left(\frac{\rm SFR_{FUV}}{M_\odot\ \rm yr^{-1}}\right) = \log_{10}\left(\frac{L_{\rm FUV}}{L_\odot}\right) - 9.69, \quad (1)$$

and is derived from the calibrations of Buat et al. (2008, 2011). Jarrett et al. (2013) combine SFR$_{\rm IR}$ and SFR$_{\rm FUV}$ to estimate a total SFR using the form

$$\rm SFR_{tot} = (1 - \eta)SFR_{IR} + SFR_{FUV}, \quad (2)$$

where η represents the fractional contribution to the total IR emission from dust reradiating energy injected from old stars; the value of 0.17 ± 0.1 is adopted (Buat et al. 2011; Jarrett et al. 2013). In the case of NGC 4565, the SFR is taken from the HALOGAS calculations in Heald et al. (2012), since no

FUV luminosities were available for these sources through *GALEX*.

The 3.4 μm band of *WISE* effectively traces light from old stars, resulting in a practical measure of the stellar mass. Jarrett et al. (2013) show a linear trend exists between *WISE W1–W2* and *W2–W3* color and stellar mass-to-light ratios (M/L). By relating the *WISE* color to 2MASS K_s in-band luminosity, a M/L ratio can be derived from the K_s stellar mass relation of Zhu et al. (2010). This trend is further explored in Cluver et al. (2014), in which the *W1–W2* color and stellar masses from the Galaxy and Mass Assembly (GAMA; Driver et al. 2009, 2011) survey are used for empirical calibration of the relationship. The best fit for their sample, including both passive and star-forming systems but excluding known active galactic nuclei sources and *WISE* colors dominated by nuclear activity (*W1–W2* $\geqslant 0.8$), is

$$\log_{10}\left(\frac{M_{*}/M_{\odot}}{L_{W1}/L_{\odot}}\right) = -1.96(W_{3.4\,\mu\mathrm{m}} - W_{4.6\,\mu\mathrm{m}}) - 0.03. \quad (3)$$

We adopt this relation to determine aggregate stellar masses for the HALOGAS sources. See Jarrett et al. (2013) and Cluver et al. (2014) for explicit details on the calculating of aggregate stellar masses utilizing *WISE* data. The adopted distance and SFRs from H11 are summarized in Table 1. See Table 2 in H11 for a complete summary of the targets' properties and an explanation of how certain target properties such as SFRs and distances were derived.

3. GBT Observations and Data Reduction, and Low-resolution WSRT Cubes

3.1. Observations and Data Reduction

Our GBT maps were made in a "basket-weave" fashion by scanning the telescope for 2°/3° along constant lines of R.A. (α_{J2000}) and decl. (δ_{J2000}) to stitch together a final 4 deg^2 (9 deg^2 for NGC 925) image (Mangum et al. 2007). If potential cold flows exist, their visibility in H I depends on how close to the disk the relatively warm gas of the flow transitions to the H I phase. For the range of distances of the sources presented in this work, the angular span of 2 deg corresponds to approximately 315–620 kpc, which are sufficient to capture a majority of the virial volume. Each row or column is offset by 3′, and each scan consisted of a total of 72 separate 5 s integrations that were dumped every 100″ to ensure Nyquist sampling. NGC 891 and NGC 925 were observed during 2010 January as part of the GBT project 10A-026, while NGC 4565 and NGC 4414 were observed during 2013 and 2014 October as part of GBT projects 13B-406 and 14B-293, respectively. We obtained an additional 10 hours to map the inner 2 × 1 deg^2 region of NGC 891 as part of GBT project 16A-411. NGC 925 and NGC 4565 were observed with the GBT Spectrometer as the backend, while the Versatile GBT Astronomical Spectrometer (VEGAS) was the backend used for the observations of NGC 4414. The observations of NGC 891 we present in this work combine the initial data from the GBT Spectrometer with the additional 10 hours of data utilizing VEGAS as the backend. During each observation, the band was centered on the H I line at the redshifts of the sources. The observing bandwidth, frequency resolution, noise at the native velocity resolution, and other data properties are summarized in Table 1. Calibration during the observation was done by frequency switching −30.0% (−23.4% for observations with VEGAS as the backend) of the total bandwidth from the center frequency at a 1 second period, and each observation session included time on 3C48, 3C147, or 3C295 as primary flux calibrator in order to compute a T_{cal} value for the noise diode. T_{cal} values computed for the Spectrometer varied between 1.53 and 1.57 K for both XX and YY polarizations with remarkably low scatter on the mean values of 1.56 and 1.57 for a period of several months ($1\sigma \sim 0.01$ K). The exceptional stability in the T_{cal} values translate to an upper limit on the uncertainty in the relative flux calibration to <1% (more on the absolute calibration below). The computed T_{cal} values for observations performed with VEGAS as the backend showed a significant decrease in the stability. We compute the mean T_{cal} for VEGAS-only observations to be 1.41 K and 1.43 K for the *YY* and *XX* polarizations, respectively, with a 1σ uncertainty equal to 0.05 K for each. The increased scatter in the VEGAS T_{cal} was likely due to a crosstalk issue in the electronics of the backend that pushed the upper limit on the absolute flux calibration slightly upward to 5%, including other systematics such as baseline removal and, to a lesser extent, T_{sys} variation. The crosstalk issue manifested itself by offseting the relative power levels between the XX and YY polarizations. This issue was fixed by the time we obtained our new data on NGC 891, and consequently only NGC 4414 data are affected. To ensure the derived T_{cal} values for VEGAS did not affect our flux calibration, we observed each HALOGAS source that used VEGAS as the backend in the fall of 2016 as part of GBT project GBT16B-393. These observations were done explicitly in position-switching mode, where the GBT was centered on source for 5 minutes, and then moved 2° in R.A. to obtain a 5-minute off-spectrum. Comparing spatially overlapping integrations between our original VEGAS data and those from the deep pointing observations showed very good agreement within the noise when the polarizations are averaged to derive the Stokes I component. We are therefore confident that the data presented here are not significantly affected by the large variation in the T_{cal} values. We still adopt an overall 5% flux uncertainty as an upper limit to account for possible errors in bandpass calibration, interference, and errors in modeling atmospheric effects. Given that the WSRT observations largely used the same calibrator sources, we are also confident in the relative flux calibrations between the two data sets. We determine the gain to be 1.86 K Jy^{-1} based on the computed T_{cal} values and an ~0.65 aperture efficiency at 1420 MHz (Boothroyd et al. 2011). The typical system temperature of observations fell between 15 and 20 K.

The frequency-switched data were reduced using a custom GBTIDL[14] routine to calculate a source temperature of the form

$$T_{\mathrm{src}} = T_{\mathrm{CAL}} \cdot \frac{P_s - \langle P_{s,\mathrm{off}} \rangle}{\langle P_{s,\mathrm{off}}^{\mathrm{CalOn}} - P_{s,\mathrm{off}}^{\mathrm{CalOff}} \rangle}, \quad (4)$$

where the quantities in brackets denote averages of four integrations from each edge of the map for a total of eight "off" integrations to increase the S/N. P_s refers to average power of the CalOn (noise diode on) and CalOff (noise diode off) states —that is, (CalOn+CalOff)/2—for a single integration in either the reference ($s = 0$) or signal ($s = 1$) bandpass switching state.

---

[14] http://gbtidl.nrao.edu/

Table 1

Summary of Observations and Properties

Source	α[a]	δ[b]	Systemic Velocity (km s^{-1})	Total Bandwidth (MHz)	$\Delta\ v$ (km s^{-1})[c]	σ (mK)[d]	d_{best} (Mpc)[e]	$\mathrm{SFR}_{\mathrm{tot}}$ ($M_{\odot}$ yr^{-1})[f]
NGC 891	$02^{\mathrm{h}}22^{\mathrm{m}}33\overset{\mathrm{s}}{.}4$	$42°20'57''$	528 ± 4	50.0	5.15	10	9.2 ± 0.9	3.92 ± 1.75
NGC 925	$02^{\mathrm{h}}27^{\mathrm{m}}16\overset{\mathrm{s}}{.}9$	$33°34'45''$	553 ± 3	50.0	5.15	12	9.1 ± 0.9	0.91 ± 0.16
NGC 4414	$12^{\mathrm{h}}26^{\mathrm{m}}27\overset{\mathrm{s}}{.}1$	$31°13'25''$	716 ± 6	23.4	5.15	13	18 ± 2	3.45 ± 1.58
NGC 4565	$12^{\mathrm{h}}36^{\mathrm{m}}20\overset{\mathrm{s}}{.}8$	$25°59'16''$	1230 ± 5	50.0	5.15	15	11 ± 1	0.67 ± 0.10

Notes.

[a] R.A. (J2000).

[b] Decl. (J2000).

[c] Velocity resolution.

[d] Final rms noise per velocity channel.

[e] Adopted distance from H11.

[f] SFRs derived from *WISE*; value for NGC 4565 taken from Heald et al. (2012).

Table 2
Summary of Data Cubes

Source	$\theta_{\rm maj}$ (arcsec)	$\theta_{\rm min}$ (arcsec)	σ (K)	S (Jy km s^{-1})	3σ $N_{\rm H\,I}$ (cm^{-2})	Δ v (km s^{-1})
NGC 891						
High-res WSRT	28.0	21.4	0.100	$(1.90 \pm 0.09) \times 10^2$	6.7×10^{19}	8.24
Conv. WSRT	546.0	546.0	0.003	$(1.91 \pm 0.09) \times 10^2$	2.0×10^{18}	8.24
Regridded GBT	546.0	546.0	0.010	$(1.93 \pm 0.09) \times 10^2$	6.8×10^{18}	8.24
NGC 925						
High-res WSRT	37.9	33.2	0.130	$(2.85 \pm 0.14) \times 10^2$	2.4×10^{19}	4.12
Conv. WSRT	546.0	546.0	0.003	$(2.84 \pm 0.14) \times 10^2$	1.8×10^{18}	4.12
Regridded GBT	546.0	546.0	0.013	$(2.96 \pm 0.15) \times 10^2$	4.0×10^{18}	4.12
NGC 4414						
High-res WSRT	39.0	33.5	0.130	$(6.2 \pm 0.3) \times 10^1$	5.2×10^{19}	4.12
Conv. WSRT	546.0	546.0	0.005	$(6.1 \pm 0.3) \times 10^1$	2.0×10^{18}	4.12
Regridded GBT	546.0	546.0	0.013	$(7.3 \pm 0.4) \times 10^1$	5.2×10^{18}	4.12
NGC 4565						
High-res WSRT	33.5	30.8	0.150	$(2.74 \pm 0.14) \times 10^2$	4.8×10^{19}	4.12
Conv. WSRT	546.0	546.0	0.004	$(2.71 \pm 0.14) \times 10^2$	1.7×10^{18}	4.12
Regridded GBT	546.0	546.0	0.015	$(2.66 \pm 0.13) \times 10^2$	7.0×10^{18}	4.12

$P_{\rm off}$ is therefore the arithmetic mean of the CalOn and CalOff states for the "off" spectrum generated from the average of the eight edge integrations in the corresponding bandpass state. Additionally, the denominator represents the average difference between CalOn and CalOff states for the corresponding switching bandpass. Equation (4) therefore calibrates our frequency-switched data as if we had position switched data. Using the edge of the map as a reference position is an advantage because we are able to obtain a reference spectrum for each R.A./decl. scan without sacrificing telescope time to slew off source. In the case of NGC 925, emission from a companion source near the edge of our map forced us to use eight contiguous integrations on the opposite map edge as our "off" position. The reference bandpass ($s = 0$) is then shifted in frequency to match the signal bandpass ($s = 1$) and arithmetically averaged to improve the noise by a factor of $\sqrt{2}$. We then fit a third-order polynomial to the emission-free regions of the spectra for all of our sources to remove baseline structure and any residual continuum sources leftover from our calibration procedure. In order to convert to units of T_A^*, we assumed a constant zenith opacity appropriate for 21 cm observations of 0.01 (Chynoweth et al. 2011). We manually flagged $< 0.5\%$ of all integrations due to broadband radio frequency interference using a custom graphical flagging GBTIDL routine. Finally, we used a boxcar smoothing function to produce raw GBT spectra at a velocity resolution of 5.15 km s^{-1}. See Wolfe et al. (2016) and the GBT technical memo Wolfe et al. (2015) for a more comprehensive discussion on the mapping sensitivity, data acquisition, and reduction.

These calibrated data were then converted to a format readable by AIPS using the IDLTOSDFITS[15] program and imported into AIPS, where they were gridded into the final raw GBT data cubes using a convolution function of a Gaussian-tapered circular Bessel function (Mangum et al. 2007) within the task SDGRD.

3.2. Convolution of WSRT Data

Accurate comparisons between high-resolution interferometer observations and single-dish observations require the interferometer data to be smoothed to the resolution of the single-dish data set. Conventional analysis approximates the single-dish beam with a Gaussian smoothing function. While this is normally a good approximation, our goal of detecting low column density material around nearby galaxies requires a more comprehensive treatment, since the Gaussian approximation for the single-dish beam does not take into account radiation coming into the near sidelobes and wings of the main beam. Since our sources are well separated from Galactic H I, we are only concerned with emission originating from H I in and near our target galaxies.

In order to account for extended emission coming into the GBT's innermost sidelobes, we construct a model beam map motivated from recent detailed simulations of the aperture illumination of the GBT at 1.4 GHz (S. Srikanth 2017, private commmunication) as part of an ongoing project to produce a measured map of the GBT power pattern. We derive the model by taking the square of the forward Fourier Transform of a simulated in-focus aperture radiation pattern. An example of our calculated beam model is shown in Figure 1 as a contoured 2D polar plot. The farthest sidelobes in this map extend out approximately 1°.2 on the sky in radius between the −40 and −50 dB level. Interestingly, the innermost sidelobes *are not* symmetric. Boothroyd et al. (2011) has thoroughly mapped the all-sky response of the GBT beam out at the farthest sidelobes. But due to system saturation effects within 1° of the Sun, the nearest sidelobes, which are most susceptible to contamination from stray radiation in this work, were not able to be accurately mapped. The model presented in that paper (see their Figure 5) showed the sidelobes were highly symmetric. Emission entering the sidelobes at ~1°.2 are not likely to contaminate our spectra, as the gain here is approximately 50 dB down from the peak of the primary beam. However, the first sidelobe is only 30 dB down from the peak response. This makes contamination possible with some sources that have strong, extended emission out to ~0°.5. We account for the possibility of contamination in the nearest sidelobes by using the GBT

---

[15] Developed by Glen Langston of NRAO; documentation at https://safe.nrao.edu/wiki/bin/view/GB/Data/IdlToSdfits.

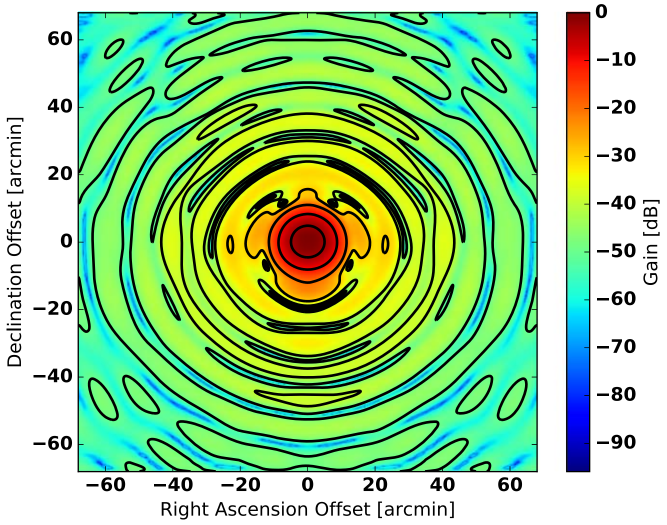

Figure 1. Normalized polar plot of a model GBT beam response on the sky. The contours represent dB levels of −3, −10, −20, −30, and −40.

model beam map to include the sidelobe geometry in the convolution of the WSRT cubes. This provides the most accurate comparison possible between the two data sets without a genuine, measured beam map of the GBT.

There are, however, subtle consequences from utilizing a beam model with a set size as a smoothing kernel for high-resolution data. Namely, the final angular resolution of the convolved data will be *slightly* coarser than the GBT data because the high-resolution data are already convolved with the WSRT clean beam. Since the GBT beam model is not strictly Gaussian, we cannot solve for the optimal size of the kernel by taking the quadrature difference between the respective full-width half maximum (FWHM) values of the GBT and WSRT clean beam. We instead employ a Fourier transform ($\mathfrak{F}$) deconvolution method, wherein the $\mathfrak{F}$ of the GBT beam model ($\mathfrak{F}[\Omega_{\rm GBT}]$) is divided by the $\mathfrak{F}$ of the WSRT clean beam ($\mathfrak{F}[\Omega_{\rm WSRT}]$) to derive an optimal smoothing kernel, $K\{{\rm WSRT} \rightarrow {\rm GBT}\}$.

We follow a similar procedure described in Aniano et al. (2011) to apply the necessary tapers that reduce numerical noise introduced by the FFT algorithm. We first taper the FT of the GBT beam with a piecewise function of the form

$$\Phi(k) = \begin{cases} 1 & \text{if } k < k_\alpha \\ \exp\left[-(1.8249 \times \left(\dfrac{k - k_\alpha}{k_\beta - k_\alpha}\right)\right] & \text{if } k_\alpha \leqslant k \leqslant k_\beta, \\ 0 & \text{if } k_\beta < k \end{cases}$$

where k_β is taken to be the spatial frequency corresponding to four times the FWHM of the GBT and $k_\alpha = 0.9k_\beta$. We refer to the tapered form of $\mathfrak{F}[\Omega_{\rm GBT}]$ as $\mathfrak{F}[\Omega_{\rm GBT}]_\Phi$. The amount of power removed from tapering the high spatial frequencies is much less than 1%, since almost all of the power is contained near spatial frequencies corresponding to the main beam. Nevertheless, it is important to ensure high spatial frequencies are near zero to avoid introducing numerical artifacts when $\mathfrak{F}[\Omega_{\rm WSRT}]$ is divided out. We then take the reciprocal of $\mathfrak{F}[\Omega_{\rm WSRT}]$ and taper the result by the low-pass filter

$$f_T(k) = \begin{cases} 1 & \text{if } k < k_{\rm L} \\ 0.5 \times \left[1 + \cos\left(\pi \times \dfrac{k - k_{\rm L}}{k_{\rm H} - k_{\rm L}}\right)\right] & \text{if } k_{\rm L} \leqslant k \leqslant k_{\rm H} \\ 0 & \text{if } k_{\rm H} < k. \end{cases}$$

Here, $k_{\rm H}$ is chosen such that $\mathfrak{F}[\Omega_{\rm WSRT}](k_{\rm H}) = 5 \times 10^{-3} \cdot \max(\mathfrak{F}[\Omega_{\rm WSRT}])$ and $k_{\rm L} = 0.7 \times k_{\rm H}$. We choose $k_{\rm H}$ as such to ensure a high spatial frequency cutoff where $\mathfrak{F}[\Omega_{\rm WSRT}]$ is still appreciable, while the form of $k_{\rm L}$ is chosen to leave a majority of the lowest spatial frequency components unaffected by the filter.

The form of the optimal kernel is therefore given as

$$K\{{\rm WSRT} \rightarrow {\rm GBT}\} = \left| \mathfrak{F}^{-1}\left[\mathfrak{F}[\Omega_{\rm GBT}]_\Phi \times \frac{f_T}{\mathfrak{F}[\Omega_{\rm WSRT}]}\right] \right|, \tag{5}$$

where $|\mathfrak{F}^{-1}|$ represents the magnitude of the inverse Fourier Transform back to the sky plane. We note that Aniano et al. (2011) worked strictly with the real components, since their kernels were largely rotationally symmetric. Since the WSRT clean beams are generally not symmetric, their Fourier Transforms will not be rotationally symmetric. As such, we work with the polar forms of $\mathfrak{F}[\Omega_{\rm WSRT}]$ and $\mathfrak{F}[\Omega_{\rm GBT}]$ to preserve the phase contribution. The resulting smoothing kernels are, as expected, *marginally* narrower than the GBT beam model, with the largest residuals ($\leqslant$0.01%) occurring toward the center.

3.3. Primary-beam Correction

The standard reduction techniques of imaging and deconvolution of interferometer data result in a model representation of the sky multiplied by the primary-beam response of the antennas. The most accurate measure of flux requires a "primary-beam correction" to the final data products, which we define as dividing out the primary-beam response of each velocity plane in the cube. We remove the primary-beam response from the native high-resolution WSRT cubes in the *Miriad* software package (Sault et al. 1995) with the same beam model used in H11. The primary-beam correction is applied before convolution, as this most accurately represents the sky distribution observed by the interferometer. Furthermore, since the resulting low-resolution data cube must be scaled by the ratio of the GBT beam to the smaller WSRT synthesized beam to account for resolution differences when measuring the total flux, we found that removing the primary-beam response after convolution does not conserve the total flux value computed for the high-resolution cube. To avoid issues with the non-uniform noise properties toward the edge, we extract a sub-cube such that all spatial scales fall within the half-power point of the WSRT primary beam for our subsequent analysis.

4. Results

4.1. Summary of Analysis

In the following section, we present initial analysis for four (NGC 891, NGC 925, NGC 4414, and NGC 4565) of the 24 total sources in the HALOGAS sample, By analyzing H I at various angular resolution and sensitivities, the extent of H I environment of these galaxies between $18 \lesssim \log_{10}(N_{\rm H\,I}/{\rm cm}^2) \lesssim 21$ can be fully characterized. Before discussing results for individual sources, we first summarize the steps of our analysis.

4.1.1. *Global* H I *Profiles and Noise*

The flux as a function of velocity measured in the three data cubes is shown in each target's respective subsection. We first use the *Miriad* task REGRID to regrid each GBT cube to be on the same angular and spectral scale as its WSRT counterpart. We estimate the noise properties within each respective cube, $\sigma(x, y)$, by fitting the negative half of a histogram whose pixels values were drawn from a region with no emission in all velocity channels (i.e., those with and without emission) with a Gaussian. We determine the 1σ noise in the native, primary-beam corrected high-resolution WSRT data cubes to be between 100 and 150 mK, between 10 mK and 15 mK for the regridded GBT cubes, and between 5 and 10 mK for the convolved, primary-beam corrected WSRT cubes. These noise properties are summarized in the fourth column of Table 2.

4.1.2. $N_{\rm H\,I}$ *Images*

Since we are mostly interested in the low column density environments of our sources, care must be taken to correctly scale the convolved data, distinguish signal from noise, as well as calculate associated uncertainties. We do this for the cumulative H I mass as a function of radius and $N_{\rm H\,I}$.

To this end, we determine the gain to convert the convolved, primary-beam corrected WSRT cubes from Jy/Beam to brightness temperature in units of Kelvin using the equation

$$T_b = \frac{\lambda^2 S}{2k\Omega_a}. \tag{6}$$

Here S is the flux density, Ω_a is the beam solid angle, k is the Boltzmann constant, and λ is the wavelength of the observation (i.e., 0.211 meters). Taking these values and simplifying, we arrive at

$$T_b[{\rm K}] = \frac{6.87 \times 10^5 S[{\rm Jy/beam}]}{\Omega_a[{\rm arcsec}^2]}. \tag{7}$$

The area of the GBT beam model used in this study is 3.69×10^5 square arcseconds, while the area of the WSRT clean beam can be approximated as a Gaussian and is given by $1.1331 \times (\theta_{\rm maj} \cdot \theta_{\rm min})$ (the major and minor axis in arcseconds, respectively). If one multiplies Equation (7) by the reciprocal of of the flux density, S, and plugs in the area of the GBT beam model, it returns the gain factor of 1.86 $[{\rm K\,Jy}^{-1}]$, as derived in Section 3.1.

Computing the noise on an individual pixel basis is imperative to the treatment of the WSRT data (at both high and low resolutions) since the primary-beam correction changes the behavior of the noise as a function of position. The noise in the GBT data is relatively uniform over the cube, though the characterization of individual pixel noise is useful for constraining uncertainties in subsequent analysis. Since the original WSRT cubes were Hanning smoothed to their final velocity resolution, the pixels along the velocity axis are not independent. Verheijen & Sancisi (2001) show an associated 1σ noise map can be computed by

$$\sigma_N(x, y) = \sqrt{\left(N(x, y) - \frac{3}{4}\right)}\frac{4}{\sqrt{6}}\sigma(x, y), \tag{8}$$

where $N(x, y)$ is the number of pixels used in the integration. For each data cube, we produce masked (where emission below some threshold is blanked) and unmasked $N_{\rm H\,I}$ images. Masked images are useful when studying the radial dependence on column density, since we wish to characterize the spatial variations of low-level signal, while unmasked images are used when studying the properties of the total flux.

We follow Verheijen & Sancisi (2001) and Lelli et al. (2014) by first constructing a mask for our high-resolution data by spatially smoothing the high-resolution cubes to 40″ (50″ in the case of NGC 4414) and only include pixels above $3\sigma(x, y)$—as determined from a fit to the negative half of a histogram—in the sum. As a consequence of this mask application, the number of channels used in the sum, and thus the uncertainty, will vary pixel-to-pixel in the resulting 1σ noise maps. Due to the variation across the map, a global 3σ-level is no longer straightforward to calculate. We calculate a global 3σ $N_{\rm H\,I}$-level in these cubes by creating a signal-to-noise (S/N) map by taking the ratio of the masked $N_{\rm H\,I}$ images with the 1σ noise maps. We then take the average of pixels in the S/N maps satisfying $2.75 \leqslant {\rm S/N} \leqslant 3.25$ to ensure a large enough sample to compute a reliable mean value. The final $N_{\rm H\,I}$ images only contain pixels whose values are above this 3σ-level. In the case of the low-resolution WSRT and GBT data, we repeat the masking procedure as described previously but directly discard pixels that do not meet the $3\sigma(x, y)$ threshold without constructing a spatially coarser cube. The beam sizes, $\sigma(x, y)$ values, total flux, the $N_{\rm H\,I}$ 3σ-level, and velocity resolutions for the data sets are summarized in Table 2.

4.1.3. *The Cumulative* H I *Mass versus* $N_{\rm H\,I}$

Since H I mass is simply proportional to column density times a physical area, and we have the distance to each source, we can convert an individual pixel value of column density to an equivalent H I mass to determine the H I mass probability distribution function, which measures the total H I contained within discrete $N_{\rm H\,I}$ bins. Integrating this distribution therefore gives the *cumulative* H I *mass as function of* $N_{\rm H\,I}$, which measures the total H I mass for pixels equal to or exceeding $N_{\rm H\,I}$ bins. This distribution conveniently describes the fraction of H I mass above and below distinct $N_{\rm H\,I}$ thresholds. We can use the cumulative H I mass distribution as a diagnostic for how well the WSRT data recover the extended H I around these sources. For example, if the GBT data detected an extended diffuse H I feature that was resolved out by the WSRT, the cumulative H I mass distribution should deviate at lower column densities. In all cases presented here, the profiles flatten out well before the $N_{\rm H\,I}$ 3σ-level listed in Table 2. We set the lowest bin to be equal to one half the listed $N_{\rm H\,I}$ value in order to avoid the inclusion of noisy pixels and focus on the behavior between low and intermediate $N_{\rm H\,I}$ levels. The maximum bin size is set to 90% of the peak $N_{\rm H\,I}$ value. Note that the cumulative H I mass as a function of $N_{\rm H\,I}$ from both telescopes is normalized by the total GBT H I mass.

One aspect of concern when analyzing low-resolution data is whether emission adequately fills the larger GBT beam. In order to simulate the effect of this analysis on an unresolved source—where the low-resolution map would simply trace the response of the GBT beam—we scale the GBT beam model introduced in Section 3.2 to the peak column density value of the GBT map and repeat the analysis calculating the cumulative H I mass as a function of $N_{\rm H\,I}$ (we do the same for the radial profiles of the of $N_{\rm H\,I}$ discussed in the next subsection). While the resolution effects will be source dependent, it is generally true that the large GBT beam does not hinder this (nor the radial average of $N_{\rm H\,I}$) analysis until the highest $N_{\rm H\,I}$ bins, which trace the structure of the main lobe.

4.1.4. Radial Profiles of $N_{\rm H\,I}$ and Cumulative Flux

The radial functions of the mean column density and cumulative flux are useful to compare how the properties of the H I emission detected by the GBT and WSRT change at various angular extents. For example, a large positive offset of cumulative flux and mean $N_{\rm H\,I}$ at large radii in the GBT data would indicate the WSRT resolved out large-scale H I emission. Additionally, profiles of the cumulative flux as a function of radius that do not flatten out or begin to dip at large radii may trace artifacts (e.g., negative bowls) in the high-resolution WSRT data. In the analysis of the radial extent of low column density structure, we use the masked $N_{\rm H\,I}$ images to ensure low-level signal has not been buried in the noise. The cumulative flux as a function of radius is derived from unmasked maps to best probe the radial variations in total flux. We also note that by measuring properties contained within radial bins overlaid on non-axisymmetric structure, the deviations at large radii inherently only reflect the distribution of H I along the major axis; thus, these plots do not reveal where potential differences between the maps occur. Nevertheless, any potential excess H I emission originating from structures spanning larger angular scales than what the WSRT is sensitive to should be evident, even in radially averaged quantities. Finally, we note that no correction for inclination angle has been applied in the computation of these radial profiles. While the inclination of our sources ranges between ∼50 deg and ∼90 deg, we are most interested in the relative difference between the profiles derived between the GBT and WSRT data sets, rather than how the radial properties change source-to-source. This relative offset between data sets for a particular source will be unaffected by the correction factor of the cosine of the inclination angle.

As a further check of resolution effects, the solid black line in the radial column density profiles again denotes the GBT beam model scaled to the peak $N_{\rm H\,I}$ value of the GBT data. Again, the model of an unresolved source deviates sufficiently well from the data, indicating this analysis is not particularly hindered by resolution effects.

4.2. NGC 891

NGC 891 is an edge-on ($i \gtrsim 89°$) Sb/SBb galaxy whose H I has been extensively studied over the past 2 decades (e.g., Sancisi & Allen 1979; Rupen 1991; Swaters et al. 1997; Oosterloo et al. 2007). Utilizing the WSRT, Oosterloo et al. (2007) made deep, high-resolution maps of NGC 891. These deep maps revealed a huge galactic halo containing 30% of the total H I mass. Other significant results from this study were the discovery of a filament extending 22 kpc in projection from the disk toward the companion, UGC 1807; counterrotating H I clouds in the halo; and differential rotation lagging with respect to the disk. Models of interactions between materials from galactic fountain activity and hot coronal gas have successfully recreated the observed velocity rotational velocity gradient (Marinacci et al. 2010; Fraternali 2017). Halo pressure gradients and magnetic tension likely contribute as well (Benjamin 2002). See Figure 2 for the masked integrated H I image and velocity fields of NGC 891 at low and high resolution. The GBT data do not reveal any low-level emission extending from NGC 891 to its companion, UGC 1807.

The global flux density profiles for NGC 891 derived from the GBT and WSRT data are shown in Figure 3(a). There is excellent consistency between the profiles. The total measured flux for the GBT data is 193 ± 9 Jy km $\rm s^{-1}$. The flux density measured by the GBT translates to a total H I mass of $(3.86 \pm 0.19) \times 10^9 M_\odot$ at the adopted distance of 9.2 ± 0.9 Mpc from H11. The flux values for the convolved and high-resolution WSRT data are measured respectively to be 191 ± 9 Jy km $\rm s^{-1}$ and 190 ± 9 Jy km $\rm s^{-1}$.

Figure 3(b) summarizes the results of the cumulative H I mass as a function of $N_{\rm H\,I}$ for NGC 891. While the cumulated H I mass distribution from the simulated point source observation falls well below the data, values computed from the unmasked GBT and convolved WSRT $N_{\rm H\,I}$ images trace each other extremely well within the estimated uncertainties.

Figure 3(c) and (d) show the radial dependence of the mean column density and cumulative flux, respectively. The radial dependence of column density in the GBT and convolved WSRT data are effectively identical within 40 kpc, indicating the GBT data do not reveal any large-scale H I features (down to the H I column density sensitivity limit) that may potentially relate to the substantial extraplanar H I component and filament observed in NGC 891. In Figure 3(d), the additional flux detected in the high-resolution WSRT data at projected scales smaller than the GBT beam (about 24 kpc at a distance of 9.2 Mpc) originates from emission that completely fills the smaller WSRT beam while remaining unresolved in the larger GBT beam. Past this point, all three data sets begin to converge to a similar value and profile shape. The dip in cumulative flux in the high-resolution profile highlights the presence of artifacts (e.g., a large-scale negative bowl caused by missing central baselines in the $u - v$ coverage, or residual sidelobes leftover from the deconvolution of the dirty beam).

The channel maps in Figure 4 show the extent of the emission detected by the GBT at the 5σ level traces the same 5σ level in the WSRT data very well. Unlike similar GBT observations of NGC 2403 (de Blok et al. 2014), another galaxy with a large H I filament, we do not detect any obvious structure associated with the 22 kpc long filament detected in the deep H I images presented by Oosterloo et al. (2007) in the individual channel maps. The agreement between the various data sets for NGC 891 in total flux, mean column density as a function of radius, and the spatial extent of emission in the individual low-resolution data channel maps show the HALOGAS data do an excellent job of recovering the full H I distribution of NGC 891; there is little difference between the H I environment at the $N_{\rm H\,I} \sim 10^{18} \rm cm^{-2}$ as compared to the $N_{\rm H\,I} \sim 10^{19} \rm cm^{-2}$ level.

4.3. NGC 925

NGC 925 is another galaxy within the HALOGAS survey whose H I distribution has been thoroughly studied over the past decades (e.g., Gottesman 1980; Pisano et al. 1998;

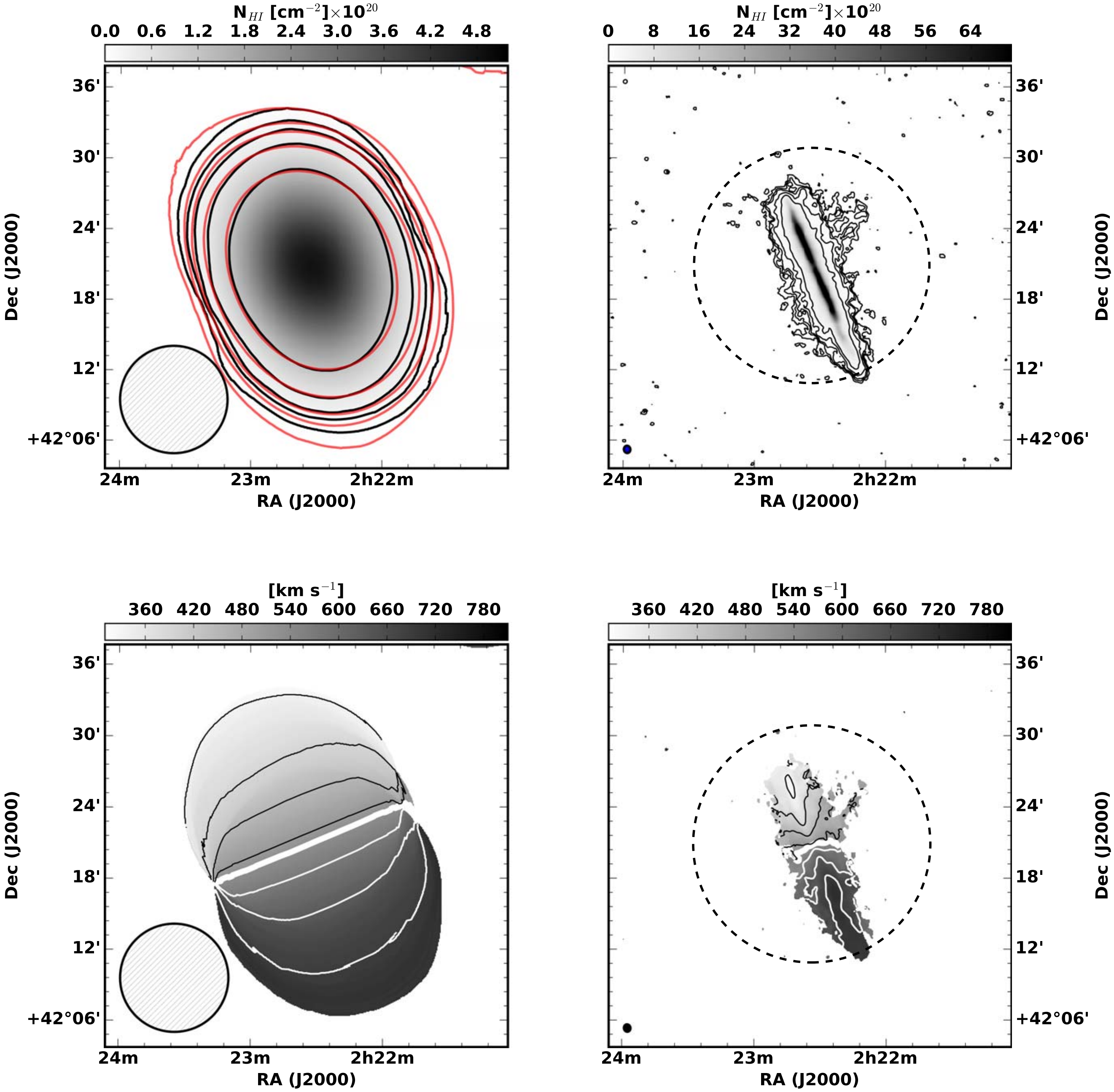

Figure 2. Integrated H I image (top) and velocity fields (bottom) for the low-resolution (left) and high-resolution WSRT (right) data for NGC 891. The contours in the low-resolution $N_{\rm H\,I}$ images start at a column density value of 5×10^{18} cm^{-2} and continue at 3, 5, 10, and 25 times that level. The black and red contours respectively denote the regridded GBT and convolved WSRT data. The contours in the associated high-resolution image begin at a level equivalent to 2×10^{19} cm^{-2} and continue at 3, 5, 10, and 25 times that level. Note that the low-resolution velocity field is derived only from the GBT data cube. The contours in both velocity fields begin at 330 km s^{-1} and continue in steps of 60 km s^{-1}. The systemic velocity of 528 km s^{-1} is represented by the thick line, and the approaching and receding velocities are denoted by black and white contours, respectively. The dashed circles in the right two panels represent the maximum recoverable angular scale of the WSRT data.

Walter et al. 2008; H11). For a galaxy such as NGC 925, which has been observed as part of both THINGS and HALOGAS, we can compare the VLA, WSRT, and GBT observations. For this comparison, we utilize the same naturally weighted, residual scaled, blanked cube used to measure the total H I flux and moment maps in Walter et al. (2008) regridded to the WSRT spatial/spectral scale and convolved to the same angular resolution. Figure 5 shows two $N_{\rm H\,I}$ images (top and middle left) of NGC 925 derived from GBT data. The expanded map shows the companion galaxy, UGC2023. There is no evidence for interacting or connecting material between NGC 925 and UGC2023 seen in the GBT data. Figure 5 also shows a comparison between the WSRT-HALOGAS (middle right) and VLA-THINGS (top right) data for NGC 925 in the form of $N_{\rm H\,I}$ images. It is clear that the more sensitive WSRT observations reveal a much more extended H I distribution than the THINGS data. This large structure ~26 kpc across, which extends from $\alpha_{\rm J2000} = 02^{\rm h}24^{\rm m}30^{\rm s}$, $\delta_{\rm J2000} = 33°17'$ to $\alpha_{\rm J2000} = 02^{\rm h}23^{\rm m}48^{\rm s}$, $\delta_{\rm J2000} = 33°12'$, is visible in the VLA-THINGS data, albeit at very low levels. As the shortest baselines in the THINGS survey are effectively equal to those in HALOGAS at 35 m, we can attribute the additional structure observed by the WSRT strictly to a lower noise floor (as opposed to differences in the maximum recoverable angular scale). Figure 5 also

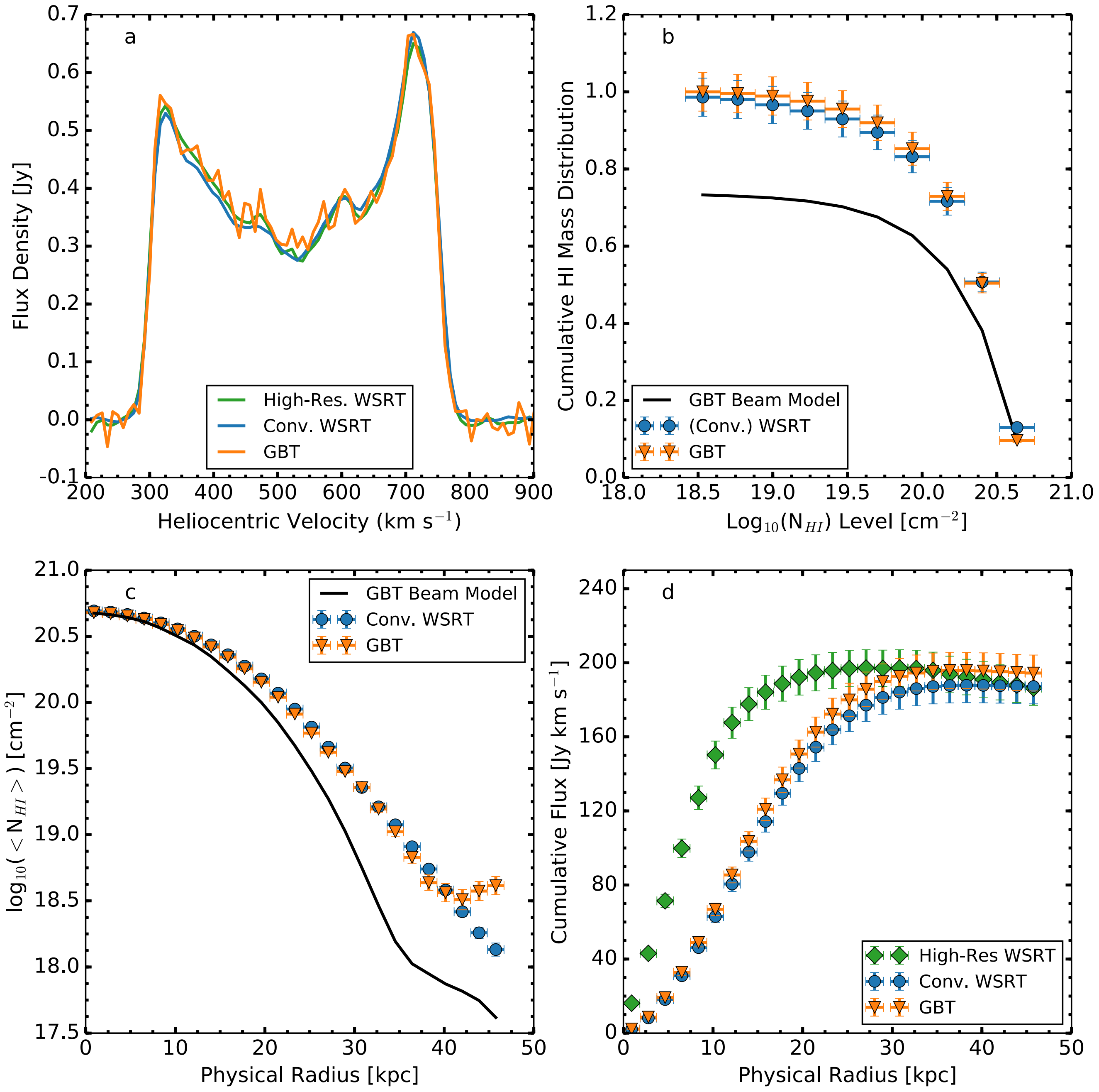

Figure 3. Comparison between the high-resolution (green diamonds) WSRT, convolved WSRT (blue circles), and regridded GBT (orange inverted triangles) data sets of NGC 891. (a) Global H I profile. (b) Cumulative H I mass as a function of $N_{\rm H\,I}$. The solid black line simulates an unresolved observation with our GBT beam model. (c) Projected physical radial dependence on the azimuthally averaged $N_{\rm H\,I}$. (d) Projected radial dependence of the cumulative flux. In this case, we also show the results of our analysis on the high-resolution WSRT data.

shows the velocity field maps computed from the GBT (bottom left) and WSRT (bottom right) data with the contour levels are given in the figure caption. The high-resolution velocity field shows deviations from axial symmetry coincident with the disturbed structure in the $N_{\rm H\,I}$, indicating a deviation from circular rotation. H11 attributes the origin to a possible interaction with a gas-rich dwarf companion seen as a faint enhancement in the Digital Sky Survey optical plates centered at about $\alpha_{\rm J2000} = 02^{\rm h}26^{\rm m}44^{\rm s}$, $\delta = 33°25'20''$.

We show the global H I profiles of NGC 925 computed over the same angular area from the GBT, VLA, and two WSRT data sets in Figure 6(a). The GBT detects more flux over approaching velocities (approximately 430–550 km s^{-1}) than the WSRT, while both the WSRT and GBT detect more flux over the entire velocity range than what is measured in VLA data.

The difference in the profiles highlights that the recovered flux detected by an interferometer is dependent on the distribution and treatment (e.g., tapering of baseline amplitudes) of the complex visibilities. For this specific THINGS cube, the visibilities were "naturally" weighted in the AIPS task IMAGR, meaning the visibilities were weighted to maximize surface brightness sensitivity. In the case of NGC 925, the

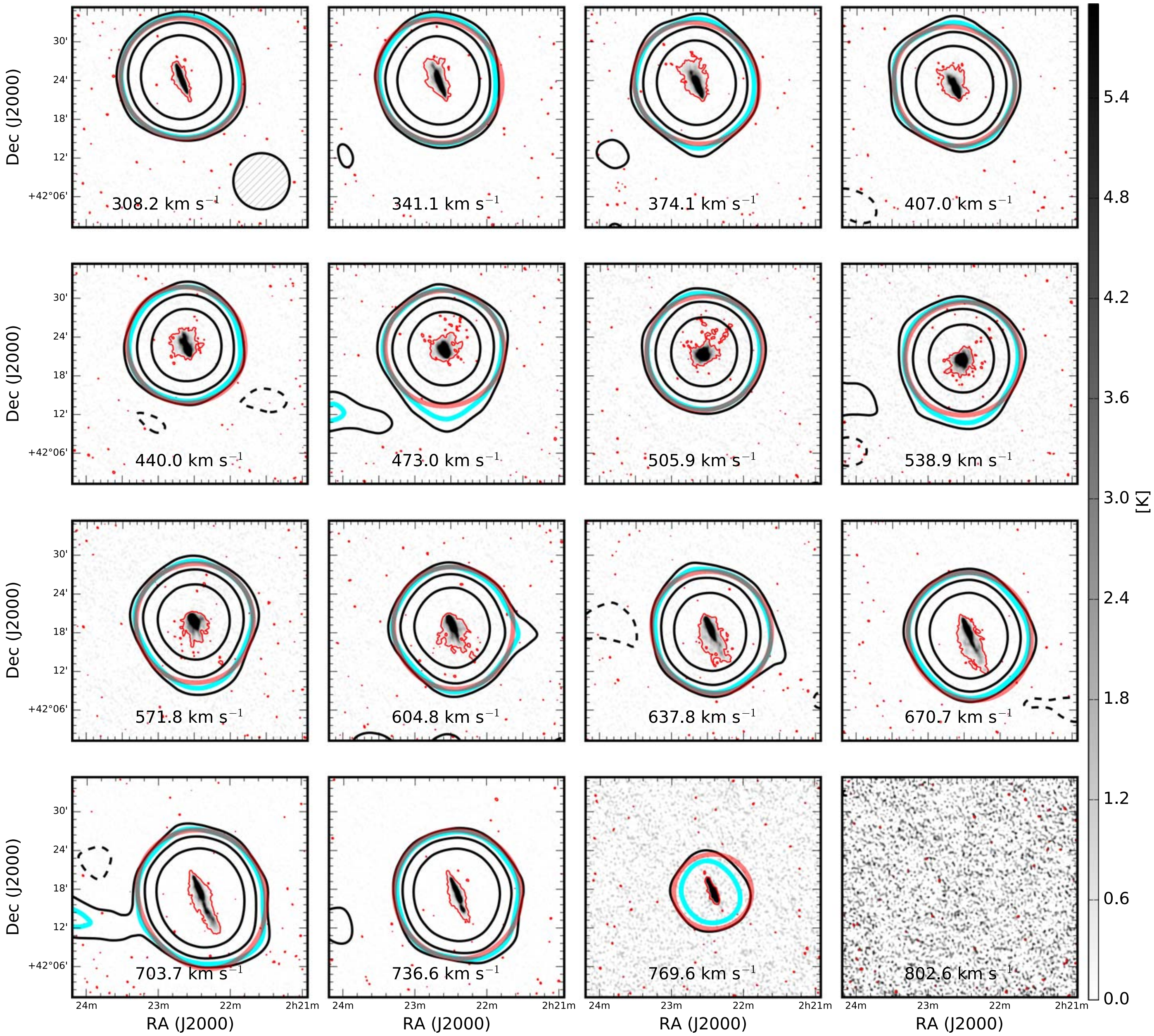

Figure 4. Selected channel maps of the NGC 891 high-resolution WSRT data cube with corresponding GBT and convolved WSRT contours superimposed. The GBT data are shown in black and cyan contours at levels of −3 (dashed), 3, 5 (thick cyan), and 25 times 0.01 K, or equivalently a column density level of 1.5×10^{17} cm^{-2} per 8.24 km s^{-1} velocity channel. The grayscale shows the H I emission from the WSRT cube. The thin red line denotes a brightness temperature of 0.4 K, or a column density level of 5.9×10^{18} cm^{-2}, and the thick red line denotes emission at 7.5×10^{17} cm^{-2} (the same level of the cyan contour) in the primary-beam corrected WSRT cube convolved down to the GBT resolution. The GBT beam is shown in the top left panel.

WSRT data were designed to maximize both sensitivity (natural—same weight) and control over the dirty beam (uniform—density), with the robust parameter set to 0 in the *Miriad* task, INVERT. An additional 30″ Gaussian taper was also applied to the higher spatial frequencies to further maximize sensitivity to faint extended emission. It is therefore a testament to the WSRT observations that approximately 20% more H I is detected as compared to the VLA data, considering both were optimized to observe extended structure. In addition to the differences in weighting schemes, the antenna positions between the VLA and WSRT cause immutable differences in $u - v$ coverage, making direct comparisons in terms of the total flux between these data sets impossible. We can therefore only conclude that, because of the agreement between both high and low-resolution WSRT and GBT flux profiles (which contains the zero-spacings information), there is excellent recovery of the diffuse H I in the WSRT-HALOGAS data for NGC 925.

The cumulative H I mass as a function of $N_{\rm H\,I}$ for NGC 925 is presented in Figure 6(b). Just as is the case with NGC 891, the cumulative H I mass as a function of $N_{\rm H\,I}$ measured by the GBT is traced reasonably well by the convolved WSRT data, with only slight hints of excess H I in the $N_{\rm H\,I}$ bins below $\log_{10}(N_{\rm H\,I}/{\rm cm}^2) = 20.5$. The radial profiles of mean column density and cumulative flux also show consistency within the calculated uncertainties and expected behavior between the high-resolution and convolved WSRT data. The slight decrease in the cumulative flux beginning at a projected physical radii 40 kpc also indicates the presence of a negative bowl in the WSRT data.

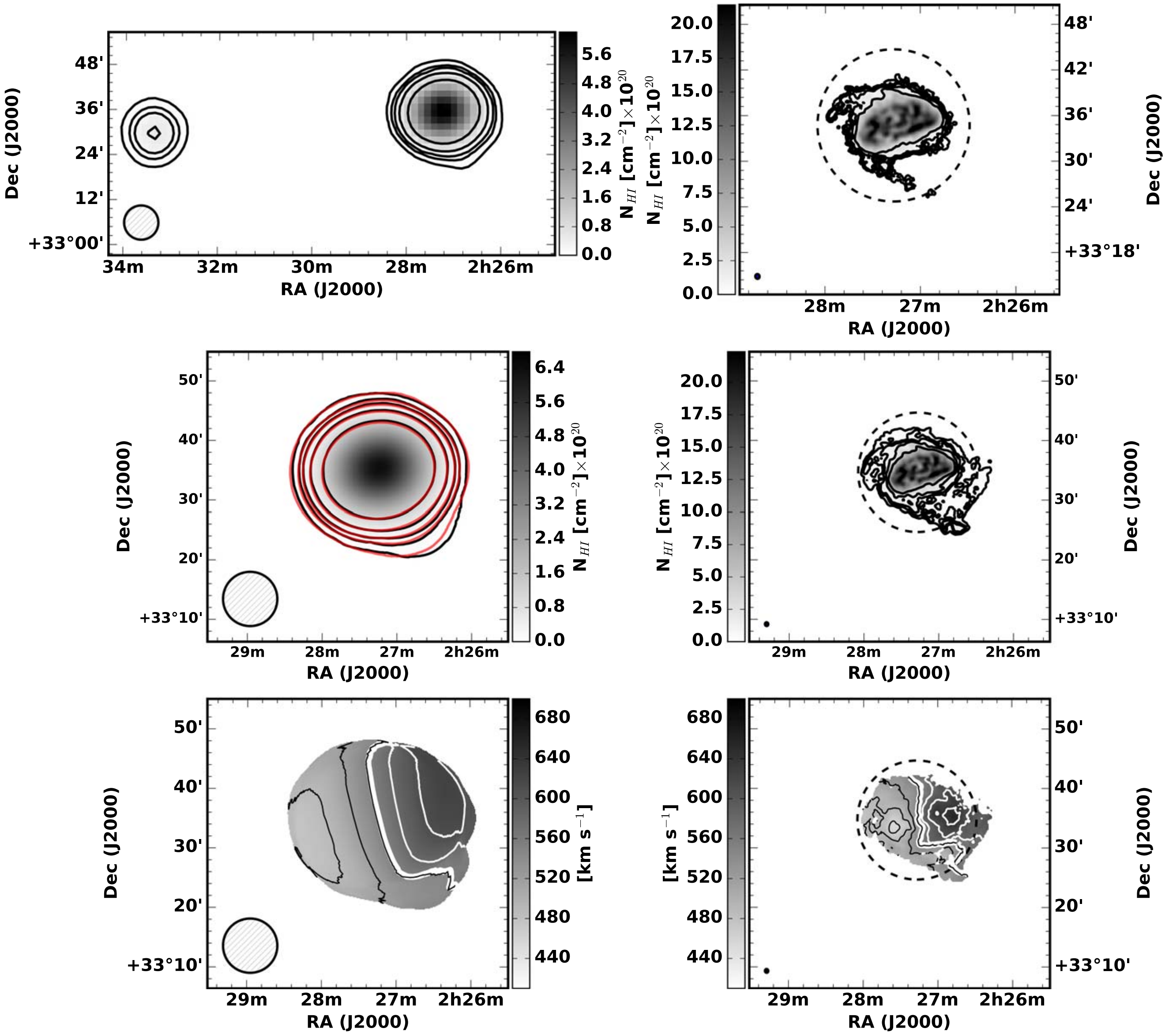

Figure 5. Comparison of several data sets for NGC 925. The top left panel shows an integrated H I map of the GBT data for NGC 925. UGC2023, a companion to the east of NGC 925, is shown in the GBT map to highlight the absence a diffuse H I bridge connecting the two galaxies. The top right panel shows an $N_{\rm H\,I}$ image computed from VLA-THINGS data. The middle and bottom left panels show a zoomed $N_{\rm H\,I}$ image of the low-resolution cubes data and GBT velocity field. The middle and bottom right panels show the $N_{\rm H\,I}$ image derived from the WSRT data and associated velocity field. The red and black contours in the low-resolution $N_{\rm H\,I}$ images respectively denote WSRT and GBT data; they begin at column density values of 5.0×10^{18} cm^{-2} and continue at 3, 5, 10, and 25 times that level, while the contour levels in the VLA and WSRT $N_{\rm H\,I}$ images begin at a $N_{\rm H\,I}$ level equivalent to 2.0×10^{19} cm^{-2} and continue at 3, 5, 10, and 25 times that level. The velocity field contours begin at 430 km s^{-1} and continue in steps of 30 km s^{-1}. The systemic velocity of 553 km s^{-1} is represented by the thick white line, and the approaching and receding velocities. The dashed circles in the right-hand panels represent the maximum recoverable angular scales of the WSRT and VLA data.

Selected channel maps of NGC 925 from the WSRT-HALOGAS data are shown in grayscale in Figure 7, with corresponding contours denoting emission from the GBT and convolved, primary-beam WSRT data overlaid. The GBT shows *slightly* more extended emission in some velocity channels. A majority of the slight extension corresponds to the velocity range of 500–600 km s^{-1}, where the disturbed H I distribution seen in the high-resolution $N_{\rm H\,I}$ images of Figure 5 is most prevalent.

Our GBT observations detect $(5.79 \pm 0.29) \times 10^9\,M_\odot$ of H I, while the WSRT data reveal $(5.54 \pm 0.28) \times 10^9\,M_\odot$ of H I measured over the same angular area. H11 found faint emission extending toward the systemic velocity (see their Figure 6). This "beard" gas is interpreted as a slowly rotating halo seen in projection against the disk with a total H I mass on the order of $10^8\,M_\odot$. While slight in magnitude, there is some emission picked up by the GBT that was missed in the original HALOGAS observations. The GBT observations therefore reveal additional H I in NGC 925 that must be some combination of extended and diffuse, as it was not detected in neither optimally weighted VLA data nor the more sensitive WSRT data. We defer correcting the WSRT data for missing short spacings for a future paper; nevertheless, a high-resolution cube that recovers emission at angular scales will provide an excellent data set for a detailed dynamical study relating the beard gas to the extraplanar component.

H11 also noted the presence of a small companion centered to the north at about $\alpha_{\rm J2000} = 02^{\rm h}27^{\rm m}20^{\rm s}$, δ=33°57′30″ in the velocity range of 613–665 km s^{-1}. This companion was cataloged as "Halogas" by Karachentsev & Kaisina (2013).

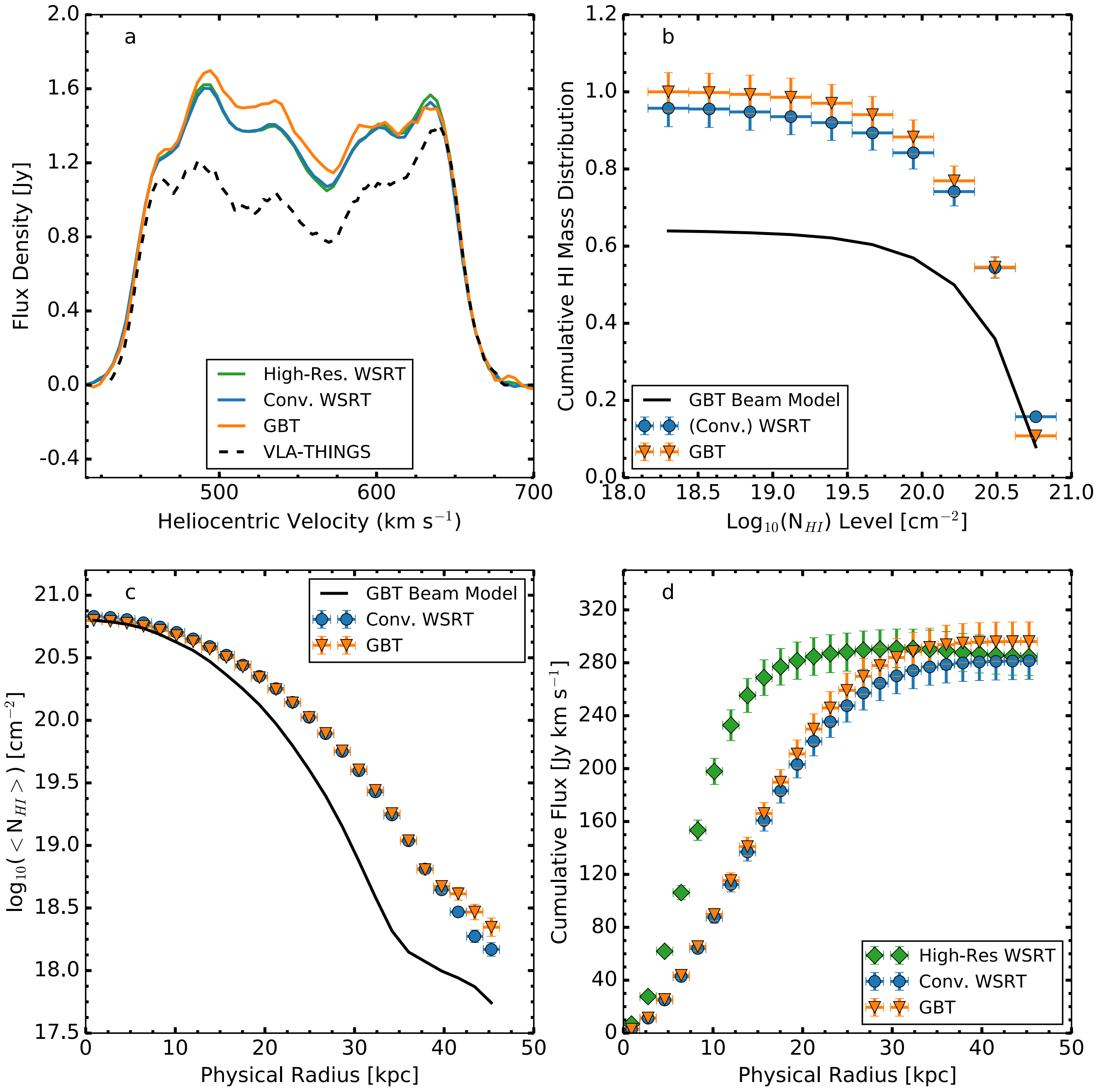

Figure 6. Comparison between the high-resolution (green diamonds) WSRT, convolved WSRT (blue circles), and regridded GBT (orange inverted triangles) data sets of NGC 925. (a) Global H I profile. (b) Cumulative H I mass as a function of $N_{\rm H\,I}$. The dashed and solid black lines simulate the contribution of a Gaussian beam and our GBT beam model, respectively. (c) Projected physical radial dependence on the azimuthally averaged $N_{\rm H\,I}$. (d) Projected radial dependence of the cumulative flux. In this case, we also show the results of our analysis on the high-resolution WSRT data.

The companion has a total H I mass (as measured by the GBT) of $(3.11 \pm 0.15) \times 10^7 \, M_\odot$, consistent with the measurement from H11. A global H I profile taken from the GBT data is shown in Figure 8; there is no detection of a bridge of H I between Halogas and NGC 925.

4.4. NGC 4414

NGC 4414 is a moderately inclined ($i = 50°$) SAc galaxy, and is one of the most distant galaxies in the HALOGAS survey at 18 ± 2 Mpc. NGC 4414 was characterized through tilted ring fitting (de Blok et al. 2014) as having a regular rotating inner disk within 240′ (∼21 kpc at the distance of NGC 4414) in radius and an outer disk that is mostly dominated by rotation with some evidence for radial and noncircular motions toward the edge of the extended H I distribution. The high-resolution WSRT-HALOGAS observations do not show any evidence for an interaction besides the disturbed outer disk, though NGC 4414 likely has undergone some weak interaction with neighboring galaxies within the Coma I cluster in the past. de Blok et al. (2014) mention a possible source of an interaction may be the small galaxy, SDSS J122646.27+311904.8, but neither the WSRT nor the GBT detect any H I at its position.

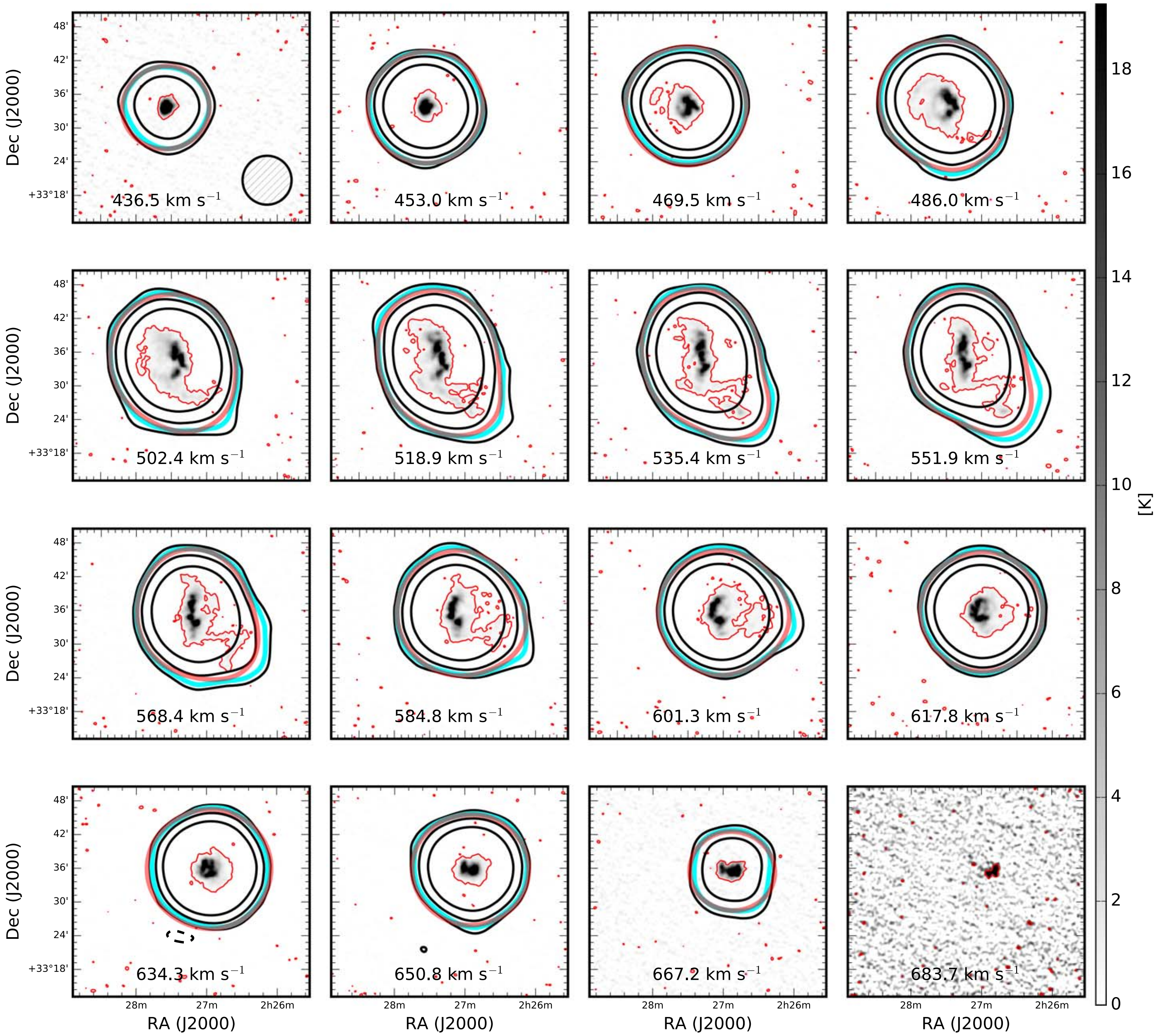

Figure 7. Selected channel maps of the NGC 925 WSRT data cube with corresponding GBT channel maps superimposed. The GBT data are shown in black and cyan contours at levels of −3 (dashed), 3, 5 (thick cyan), and 25 times 0.01 K, or equivalently a column density level of 9.75×10^{16} cm^{-2} per 4.12 km s^{-1} velocity channel. The grayscale shows the H I emission from the WSRT cube. The thin red line denotes a brightness temperature of 0.36 K, or a column density levels at 2.70×10^{18} cm^{-2}, and the thick red line denotes emission at 4.88×10^{18} cm^{-2} (the same level of the cyan contour) in the primary-beam corrected WSRT cube convolved down to the GBT resolution. The GBT beam is shown in the top left panel.

A comparison between the GBT and WSRT data is shown in Figure 9 in the form of integrated H I intensity and velocity field maps. As noted by de Blok et al. (2014), the inner regions of the velocity field show very well-behaved rotation in the inner regions of the galaxy, with motions deviating from circular toward the edge of the H I disk. These areas of irregular rotation overlap well with the presence of the disturbed structure seen in the high-resolution WSRT $N_{\mathrm{H\,I}}$ image, which again may be evidence for a past interaction. The extent of the overall H I distribution is within the maximum recoverable angular scale, as denoted by the dashed circles.

The global flux density profiles of NGC 4414 derived from the GBT and WSRT data are shown in the top left panel of Figure 10. The GBT detects more flux overall, and excess flux is encountered over almost the entire velocity range. The total H I mass measured by the GBT is $(5.43 \pm 0.27) \times 10^9\ M_\odot$, which is $\sim 1 \times 10^9\ M_\odot$ more H I than is measured in the WSRT data over the same area. The large offset in the fluxes may be due, in part, to a large plume of H I extension to the west, which is further evidence for a past interaction.

The cumulative H I mass as a functions of $N_{\mathrm{H\,I}}$ calculated from both data sets for NGC 4414 are summarized in the top right panel. The convolved WSRT data begin to trace the simulated unresolved observation quite well past $\log_{10}(N_{\mathrm{H\,I}}/\mathrm{cm}^2) = 19.0$. The offset of ∼15% between the two data profiles at the lower $N_{\mathrm{H\,I}}$ bins indicates that the WSRT observations may resolve out a

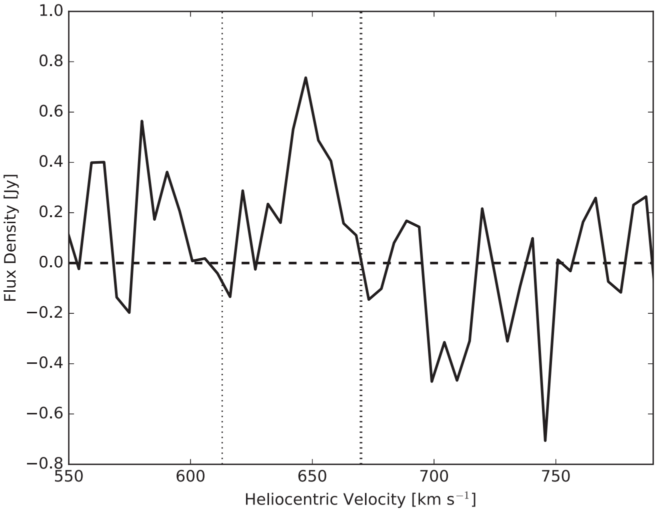

Figure 8. Global H I profile derived from GBT data for the northern companion of NGC 925 deemed "Halogas" by Karachentsev & Kaisina (2013).

structure that extends past the maximum recoverable angular scale with a peak $N_{\rm H\,I}$ on the order of $\sim 10^{18}$ cm^{-2}.

The radial dependent properties are shown in the lower two panels of Figure 10. The azimuthally averaged $N_{\rm H\,I}$ profiles interestingly begin to differ at a projected physical of about 60 kpc, while a prevalent dip in the cumulative flux profiles of the WSRT data begins near 45 kpc. Considering the $N_{\rm H\,I}$ profiles are derived from masked $N_{\rm H\,I}$ images, the deviation between the GBT and WSRT profiles could reflect the presence of artifacts, such as leftover residual sidelobes from deconvolution, that increase noise properties at larger angular extents to mimic the presence of legitimate signal. The variations in the WSRT cumulative flux profiles explicitly demonstrate the presence of artifacts in these data cubes.

Channel maps of NGC 4414 similar to Figures 4 and 7 are presented in Figure 11. The outermost 3σ contour generally extends past the 5σ contour of the convolved WSRT data in each selected velocity channel. This is consistent with the behavior of the global H I profile from Figure 10. The channel maps reveal the extent of the NGC 4414 emission in a single velocity channel is within the angular sensitivity limit ($\sim 20'$, or $\sim$ 100 kpc at the distance of NGC 4414) in the WSRT data. Additionally, the angular extent of NGC 4414 is only a few times the GBT beam area, as evidenced by the steep drop in the cumulative H I mass function. Considering all these factors, we conclude that a majority of the excess emission detected by the GBT is likely due to artifacts (e.g., residual sidelobe structure) in the WSRT cubes, as opposed to resolved-out structure.

de Blok et al. (2014) noted in their analysis that gas at velocities lower than the local rotational velocity (i.e., "beard" gas) is present in both the receding and approaching sides of the rotation curve for the inner disk of NGC 4414, and should be interpreted as extraplanar gas in the inner disk. Through a variety of techniques, including blanking high column density pixels and subtracting Gaussian fits of the velocity profiles within the observed data cube (Fraternali et al. 2002), de Blok et al. (2014) determined the H I mass of the extraplanar gas associated with the inner disk to be between 2% and 6.5% of the total H I mass of the inner disk (i.e., about $2 \times 10^8\,M_\odot$). Similarly, the authors concluded the extraplanar gas associated with the outer disk to be about 1%–2% of the total H I mass of the system. In the future, merging the GBT and WSRT data sets will provide an excellent basis for characterizing dynamical links between anomalous velocity gas and an extraplanar component in NGC 4414, as well as characterizing the kinematics of a potential past interaction.

4.5. NGC 4565

NGC 4565 is a large, edge-on SAb galaxy with two very nearby companion galaxies: IC 3571 directly to the north and NGC 4562 to the southwest; only NGC 4562 is partially resolved in our GBT data. The apparent connection is due to the beam confusion stemming from the large GBT beam. The SFR for NGC 4565 is among the lowest in the entire HALOGAS sample at 0.67 $M_\odot$ yr^{-1}. The $N_{\rm H\,I}$ images and velocity fields derived from both the GBT and WSRT data sets are detailed in Figure 12. These specific HALOGAS observations for NGC 4565 have been discussed by Zschaechner et al. (2012) and expose a potential interaction between IC 3571 and NGC 4565, as evidenced by the possible tidal material shown as a separate cloud complex between IC 3571 and the disk of NGC 4565 in the top right panel of Figure 12. It remains unclear if this structure is related to tidal interactions between the main disk of NGC 4565 and IC 3571, or an accretion process.

The total H I measured in the GBT data over the same angular region as the WSRT data (including companions) is $(7.46 \pm 0.39) \times 10^9\,M_\odot$, while the primary-beam corrected WSRT data convolved to the GBT resolution gives $(7.32 \pm 0.37) \times 10^9\,M_\odot$. The H I profiles are shown in Figure 13 and match extremely well.

The cumulative H I mass as a function of $N_{\rm H\,I}$ for NGC 4565 is presented in Figure 13(b). Both distributions also trace each other remarkably well within statistical uncertainties. Additionally, the excellent agreement between all NGC 4565 data sets extend to the mean radial column density/cumulative flux. The slight offsets toward higher projected physical radii can be attributed to a residual baseline structure in the GBT cube.

Selected channels are shown in Figure 14 with the GBT and WSRT superimposed on the high-resolution WSRT channels. The 5σ level of emission detected from the GBT is consistent with the same level in the convolved WSRT data.

The consistency in the various profiles of Figure 13 and contours in Figure 14 indicate there is no extended diffuse H I reservoir around NGC 4565 at the $N_{\rm H\,I}$ levels of $\sim 10^{18}$ cm^{-2}. Zschaechner et al. (2012) also did not find evidence using the same high-resolution WSRT data of any significant amount of extraplanar H I. The authors of that study proposed this absence is due to no significant disk-halo cycling of material in NGC 4565. The lack of any sort of extended low column density H I component supports this conclusion.

5. Discussion

In this section we will first discuss our initial survey results in the context of future H I surveys planned for forthcoming radio telescopes. The second subsection explores methods to link the diffuse environment of the HALOGAS galaxies to intrinsic galaxy properties and thus the theoretical predictions from simulations.

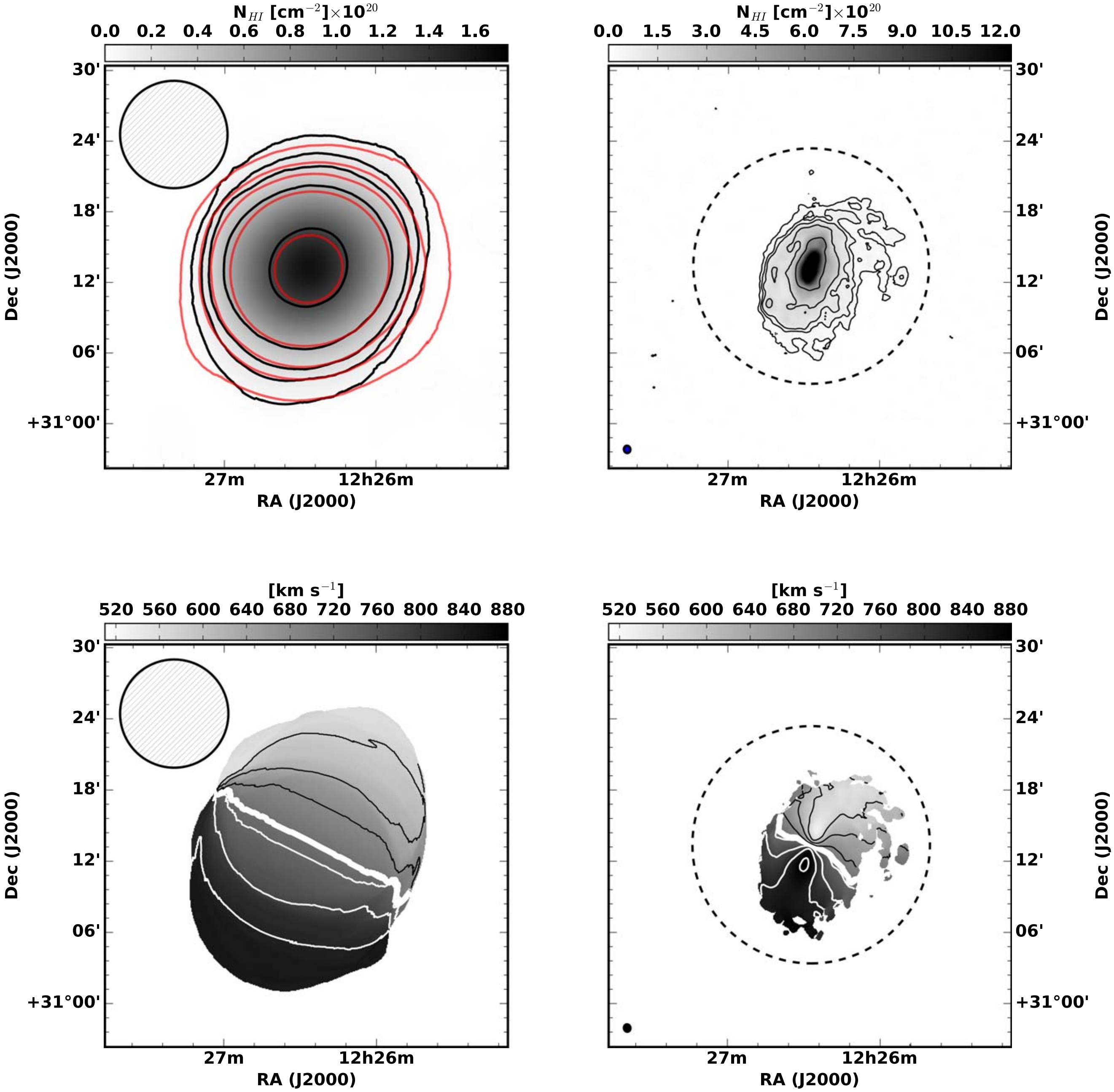

Figure 9. Comparison of the $N_{\rm H\,I}$ images (top) and velocity fields (bottom) of NGC 4414 derived from the GBT (left) and WSRT-HALOGAS (right) data. The red and black contours in the low-resolution $N_{\rm H\,I}$ images respectively denote WSRT and GBT data; they begin at a $N_{\rm H\,I}$ level of 5.0×10^{18} cm^{-2} and increase by factors of 3, 5, 10, and 25. The contours in the high-resolution WSRT $N_{\rm H\,I}$ image begin at an $N_{\rm H\,I}$ level of 2.0×10^{19} cm^{-2} and increase by factors of 3, 5, 10, and 25. The velocity contours in both maps begin at 530 km s^{-1} and increase by 50 km s^{-1}, with the systemic velocity of NGC 4414 of 716 km s^{-1} represented by the thick white contour. The receding and approaching sides are denoted by white and black contours, respectively. The GBT (WSRT) beams are shown for their respective data sets in the top (bottom) left corner of each panel. The dashed circles in the right-hand panels represent the maximum recoverable angular scales of the WSRT data.

5.1. Implications for Future H I *Surveys*

It is well known through a combination of models (e.g., Maloney 1993; Dove & Shull 1994; Bland-Hawthorn et al. 2017) and observations (van Gorkom 1996) that the transition from optically thick to optically thin medium decreases the efficiency of self-shielding, leading to a dramatic drop in the fraction of H I to total hydrogen (i.e., neutral fraction), primarily due to UV and X-ray background radiation. This effect is demonstrated in cosmological simulations of the H I distribution (e.g., Popping et al. 2009; Rahmati et al. 2015; Marinacci et al. 2017); in particular, Popping et al. (2009) shows the neutral fraction drops from 1 unity to 0.01 (or 100% to 1%) between $18.0 < \log_{10}(N_{\rm H\,I}/{\rm cm}^2) < 20.0$. This rapid decrease results in a plateau in the H I distribution function that effectively predicts the probability of detecting substantial H I structures at $N_{\rm H\,I} \sim 10^{18}$ cm^{-2} is very low, even with deep surveys. The flux as a function of velocity, cumulative H I mass as a function of $N_{\rm H\,I}$, and azimuthally averaged profiles of column density and cumulative flux show that, overall, the WSRT observations do an excellent job of recovering the low-level H I. Save for NGC 4414, we see that the H I distributions do not significantly differ between $N_{\rm H\,I} \sim 10^{18}$ cm^{-2} and $\sim 10^{19}$ cm^{-2}.

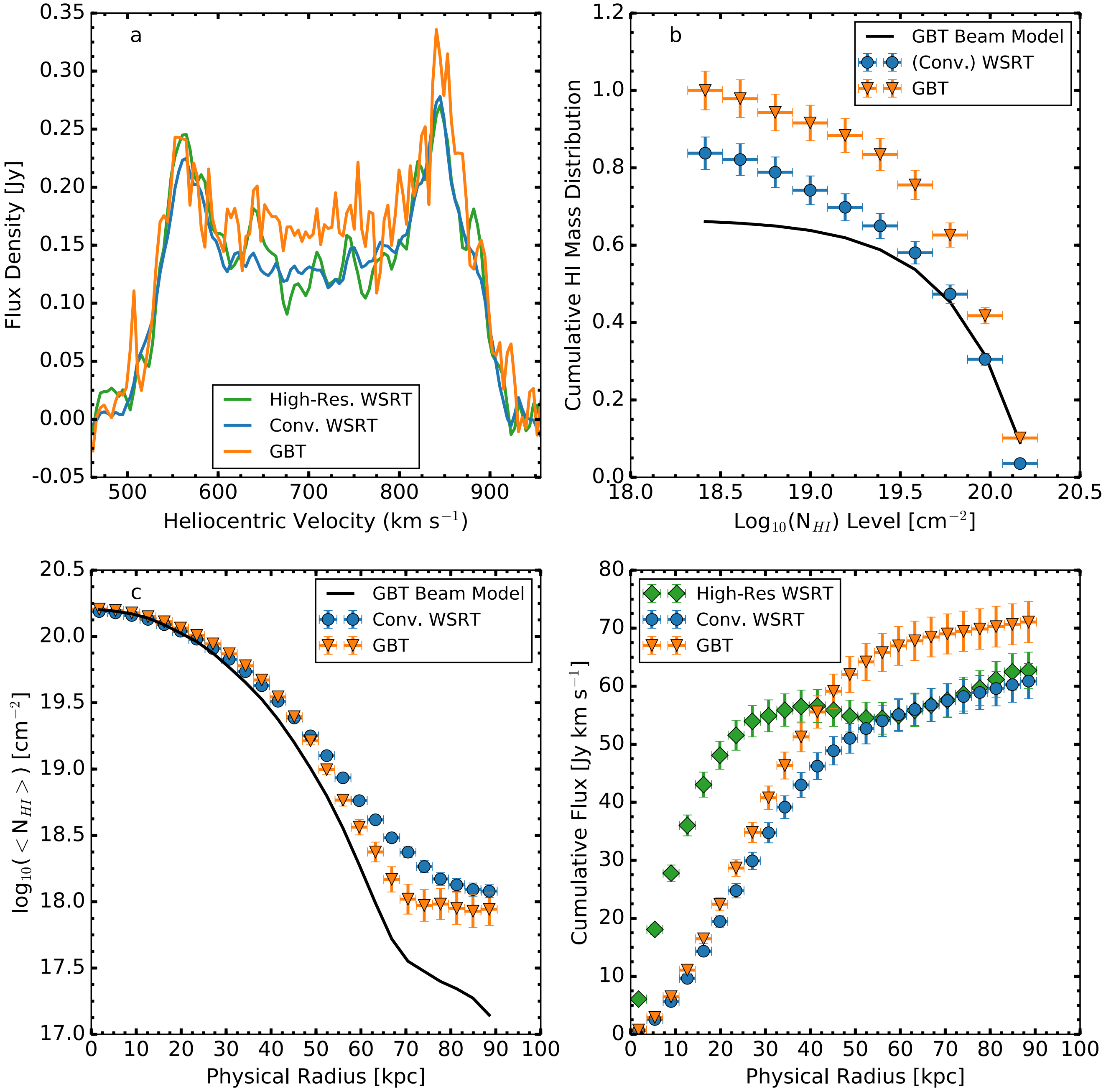

Figure 10. Comparison between the high-resolution (green diamonds) WSRT, convolved WSRT (blue circles), and regridded GBT (orange inverted triangles) for NGC 4414. (a) Global H I profile. (b) Cumulative H I as a function of $N_{\rm H\,I}$. The dashed and solid black lines simulate the contribution of a Gaussian beam and our GBT beam model, respectively. (c) Projected physical radial dependence on the azimuthally averaged $N_{\rm H\,I}$. (d) Projected radial dependence of the cumulative flux. In this case, we also show the results of our analysis on the high-resolution WSRT data.

The dearth of diffuse H I around these sources has intriguing implications on both the search for cold flow accretion and the determination of the edge of disk gas in late-type galaxies. Many simulations (e.g., Birnboim & Dekel 2003; Kereš et al. 2005, 2009) have predicted that less massive galaxies at low redshift will replenish gas through the form of cold filaments that penetrate the halo down to the disk edge where some fraction of the gas should cool sufficiently to be neutral. Aside from characterizing gas accretion mechanisms, deep H I observations are also useful for tracing large-scale structure in the local universe. Simulations undertaken by Nuza et al. (2014) predict M31 and Milky Way analogues to sit within a clumpy yet very diffuse neutral component with H I masses on the order of $\sim 10^8\,M_\odot$ existing predominately above $N_{\rm H\,I} \sim 10^{17}$ cm^{-2}. Our cumulative H I mass as a function of $N_{\rm H\,I}$ plots are consistent with this prediction. On average, only 2% of the total H I mass exists in column densities below 1×10^{19} cm^{-2} as measured in the low-resolution data sets (see Section 5.2). Given the results of Popping et al. (2009), in which the H I surface area distribution function is predicted to steepen at $N_{\rm H\,I}$ levels lower than 10^{18} cm^{-2}, we expect the offset between the GBT and WSRT cumulative H I distributions would widen considerably with the detection of diffuse H I that traces the large-scale structure of the cosmic web, an extended reservoir of diffuse neutral H I, and/or cold flow filaments at the 10^{18} cm^{-2} column density level. Such

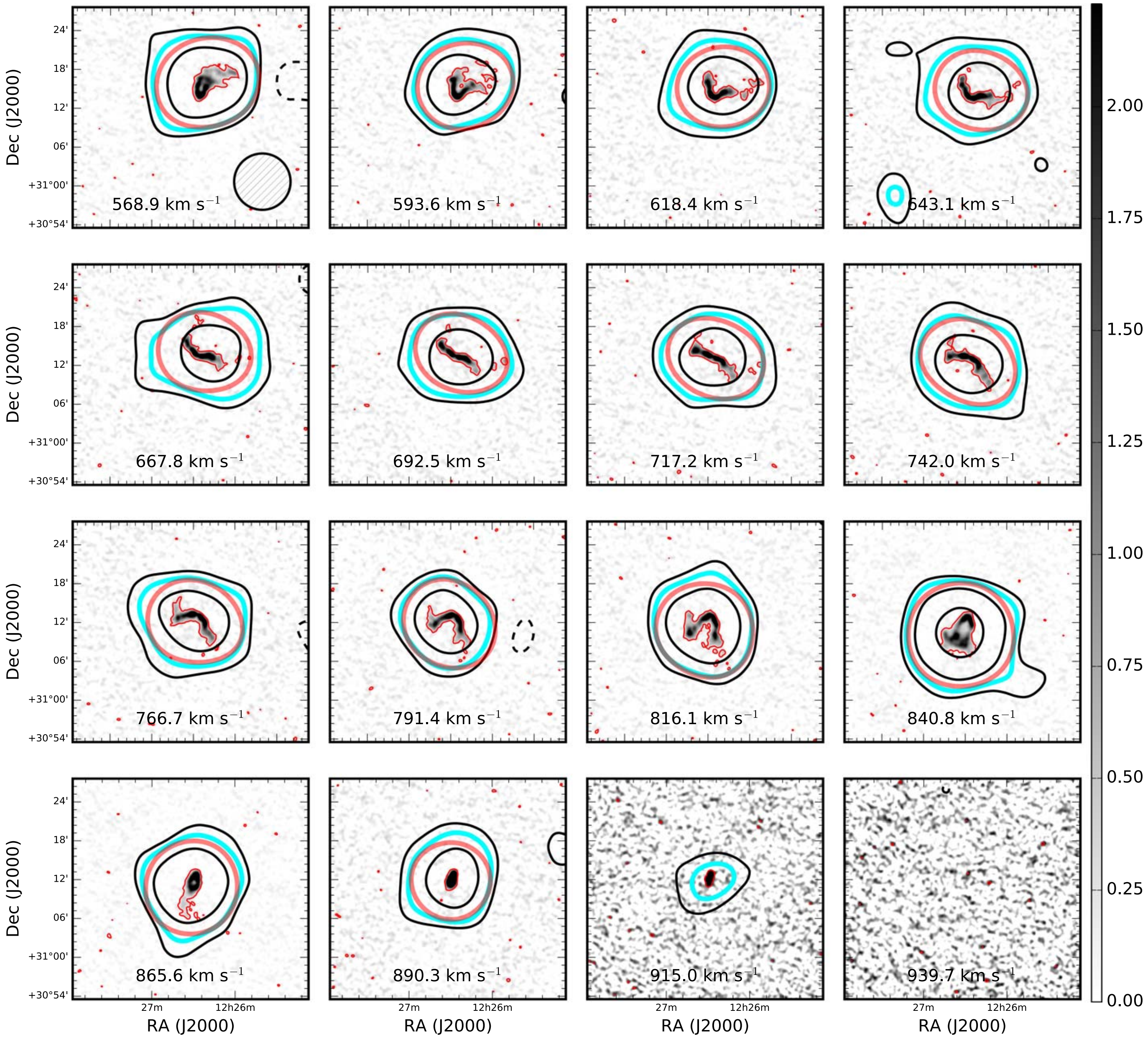

Figure 11. Selected channel maps of the NGC 4414 WSRT data cube with corresponding GBT channel maps superimposed. The GBT data are shown in black and cyan contours at levels of −3 (dashed), 3, 5 (thick cyan), and 25 times 0.01 K, or equivalently a column density level of 9.75×10^{16} cm^{-2} per 4.12 km s^{-1} velocity channel. The grayscale shows the H I emission from the WSRT cube. The thin red line denotes a brightness temperature of 0.39 K, or a column density level at 2.92×10^{18} cm^{-2}, and the thick red line denotes emission at 2.93×10^{17} cm^{-2} (the same level of the cyan contour) in the primary-beam corrected WSRT cube convolved down to the GBT resolution. The GBT beam is shown in the top left panel.

structures would likely be resolved out in an interferometric data set and therefore not contribute at all to the cumulative H I mass at these low $N_{\rm H\,I}$ levels.

Detailed analysis of the high-resolution HALOGAS H I data by E. Jütte (2018; in preparation) reveal only a few newly detected H I clouds that may be accreting. Furthermore, maps produced by Wolfe et al. (2016) of the apparent connection between M31 and M33 original discovered by Braun & Thilker (2004), which go several times deeper in column density than our observations, reveal only discrete clouds of H I with masses on the order of $\sim 10^5\,M_\odot$ as opposed to a continuous, smooth diffuse component. These early high-resolution results, coupled with the small amount of newly detected H I in the initial GBT data, suggest that if these galaxies are currently accreting gas, most of it must be ionized and unobservable in H I emission. The absence of significant H I structure at the $N_{\rm H\,I}$ level of 10^{18} cm^{-2} supports the notion that H I surveys of external galaxies must go *at least* as deep as $N_{\rm H\,I} \sim 10^{17}$ cm^{-2} to substantially increase the probability of detecting emission associated with the IGM and/or cold mode accretion.

5.2. The Relationship between Diffuse H I *and Cold Mode Accretion*

While the GBT data do not reveal new features below the $N_{\rm H\,I} \sim 10^{18}$ cm^{-2} level, as the remaining data are analyzed, it is still important to consider the implications of potential diffuse features and their relation to cold flows as predicted from simulations. Namely, how would diffuse H I related to

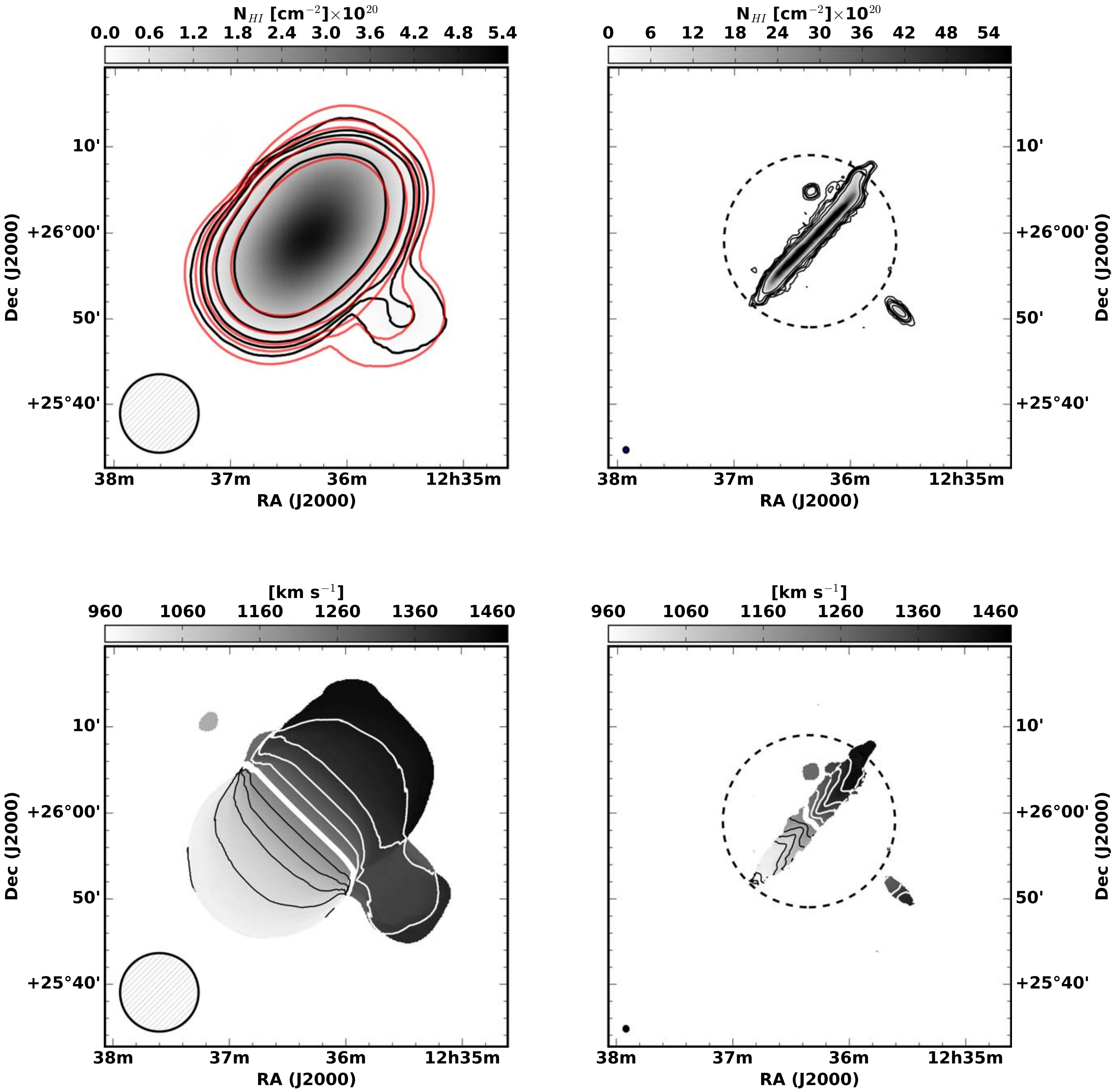

Figure 12. $N_{\text{H I}}$ images (top) and velocity fields (bottom) for GBT (left) and WSRT (right) data for NGC 4565. The red and black contours in the low-resolution $N_{\text{H I}}$ images respectively denote WSRT and GBT data. The contours start at a column density value of 5×10^{18} and continue at 3, 5, 10, and, 25 times that level in the GBT image. The contours in the associated high-resolution WSRT image begin at a level equivalent to 2.0×10^{19} cm^{-2} and continue at 3, 5, 10, and 25 times that level. The contours in both velocity fields begin at 970 km s^{-1} and continue in steps of 50 km s^{-1}. The systemic velocity of 1230 km s^{-1} is represented by the thick line, and the approaching and receding velocities are denoted by black and white contours, respectively. The dashed circles in the right-hand panels represent the maximum recoverable angular scales of the WSRT data.

cold mode accretion manifest itself in emission? Does the diffuse gas originate from outflows, tidal interactions with nearby companions, or accretion from the IGM?

To explore the relationship between the diffuse H I around nearby galaxies and simulation predictions, we measure the diffuse H I mass fraction as defined by

$$f_{19} = 1 - \frac{M_{19}}{M_{\text{H I}}}, \tag{9}$$

where $M_{\text{H I}}$ is the total H I mass detected for that particular telescope (taken from pixels with $N_{\text{H I}}$ values at and above the 3σ detection limit listed in Table 2 to avoid measuring into the noise) and M_{19} is the H I mass above the $N_{\text{H I}}$ level of 1×10^{19} cm^{-2} in the unmasked GBT and convolved WSRT $N_{\text{H I}}$ images.

The purpose of this parameter is to measure the mass fraction of diffuse H I associated with a given galaxy. We can then relate the presence (or dearth) of diffuse H I to properties predicted by cosmological simulations to correlate with higher rates of cold mode accretion. In the context of our subsequent discussion, we define diffuse H I to first be below the $N_{\text{H I}}$ level of 1×10^{19} cm^{-2}, which is on the same order as the analytical critical column densities derived by Bland-Hawthorn et al. (2017),

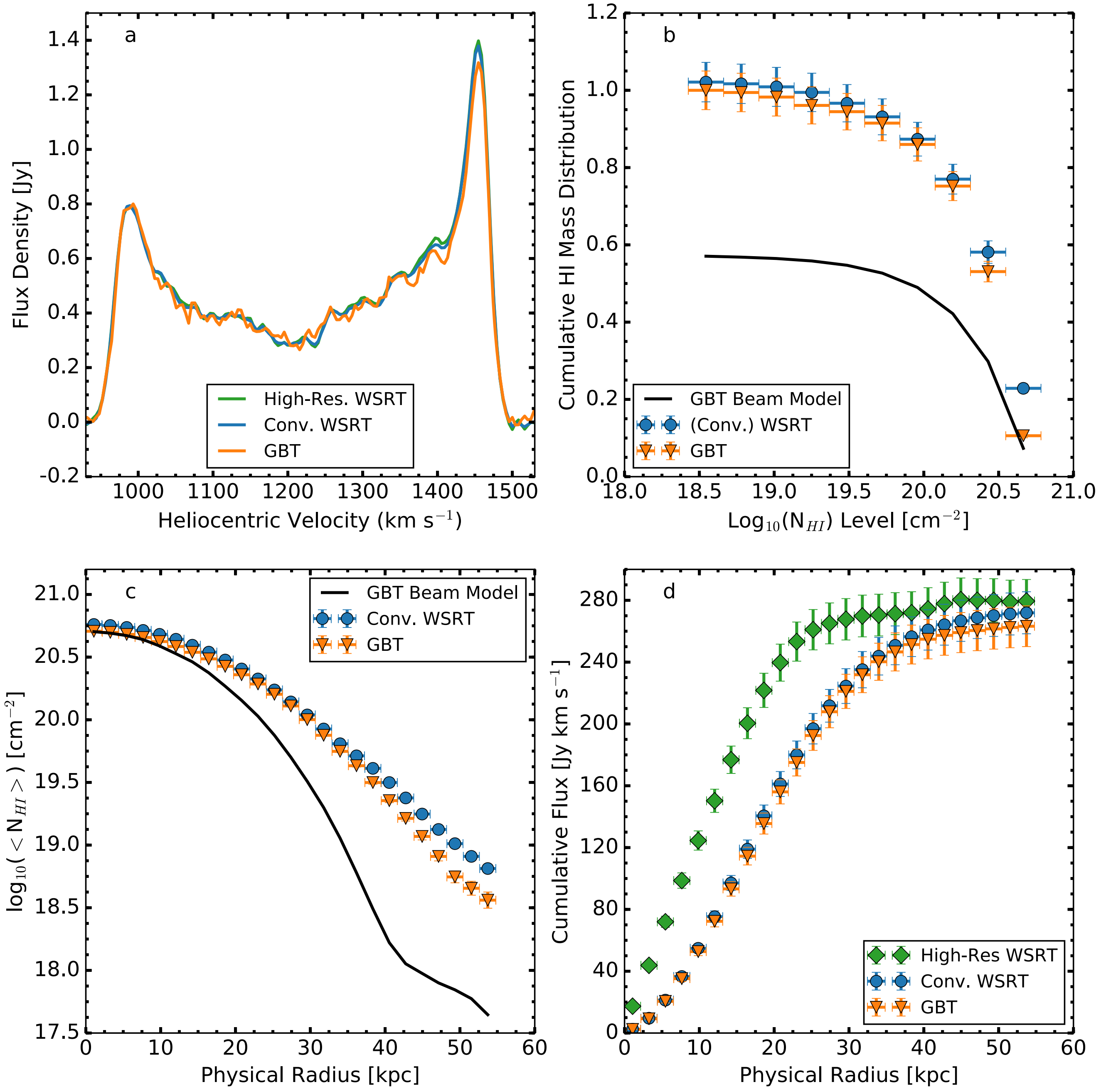

Figure 13. Comparison between the high-resolution (green diamonds) WSRT, convolved WSRT (blue circles), and regridded GBT (orange inverted triangles) for NGC 4565. (a) Global H I profile. (b) Cumulative H I mass as a function of $N_{\rm H\,I}$. The dashed and solid black lines simulate the contribution of a Gaussian beam and our GBT beam model, respectively. (c) Projected physical radial dependence on the azimuthally averaged $N_{\rm H\,I}$. (d) Projected radial dependence of the cumulative flux. In this case, we also show the results of our analysis on the high-resolution WSRT data.

Maloney (1993), and Dove & Shull (1994; i.e., where the H I transitions from mostly neutral to mostly ionized) and is approximately the 5σ $N_{\rm H\,I}$ detection limit of the native resolution WSRT data over a 20 km s^{-1} line. Second, diffuse H I is implied to be extended over angular scales larger than the maximum recoverable angular scale of the WSRT ($\sim$20′). A lower f_{19} value measured for a well-resolved source (relative to the larger GBT beam) would therefore demonstrate that most of the H I resides at higher column densities, indicating no signs of a diffuse inflowing component that can be observed in emission. On the other hand, a higher f_{19} value would suggest the WSRT resolves out large-scale H I features that possess $N_{\rm H\,I}$ levels lower than $\sim$10^{19} cm^{-2}.

Because $N_{\rm H\,I}$ is directly proportional to the measured brightness temperature, which is itself averaged over the beam solid angle, the usefulness of the f_{19} parameter to characterize the diffuse H I mass fraction relies on the sources being well-resolved. Once the source becomes unresolved, our measurement—which is effectively the convolution of the true H I emission distribution with the larger beam—will spread the flux of the out to angular scales where the beam response is lower, thus measuring low column density values that are no longer physical but nevertheless begin to dominate the overall H I mass fraction and bias our quantity. While f_{19} provides a quantity that can be related to properties predicted to be influential to accretion, given that the sources presented in this

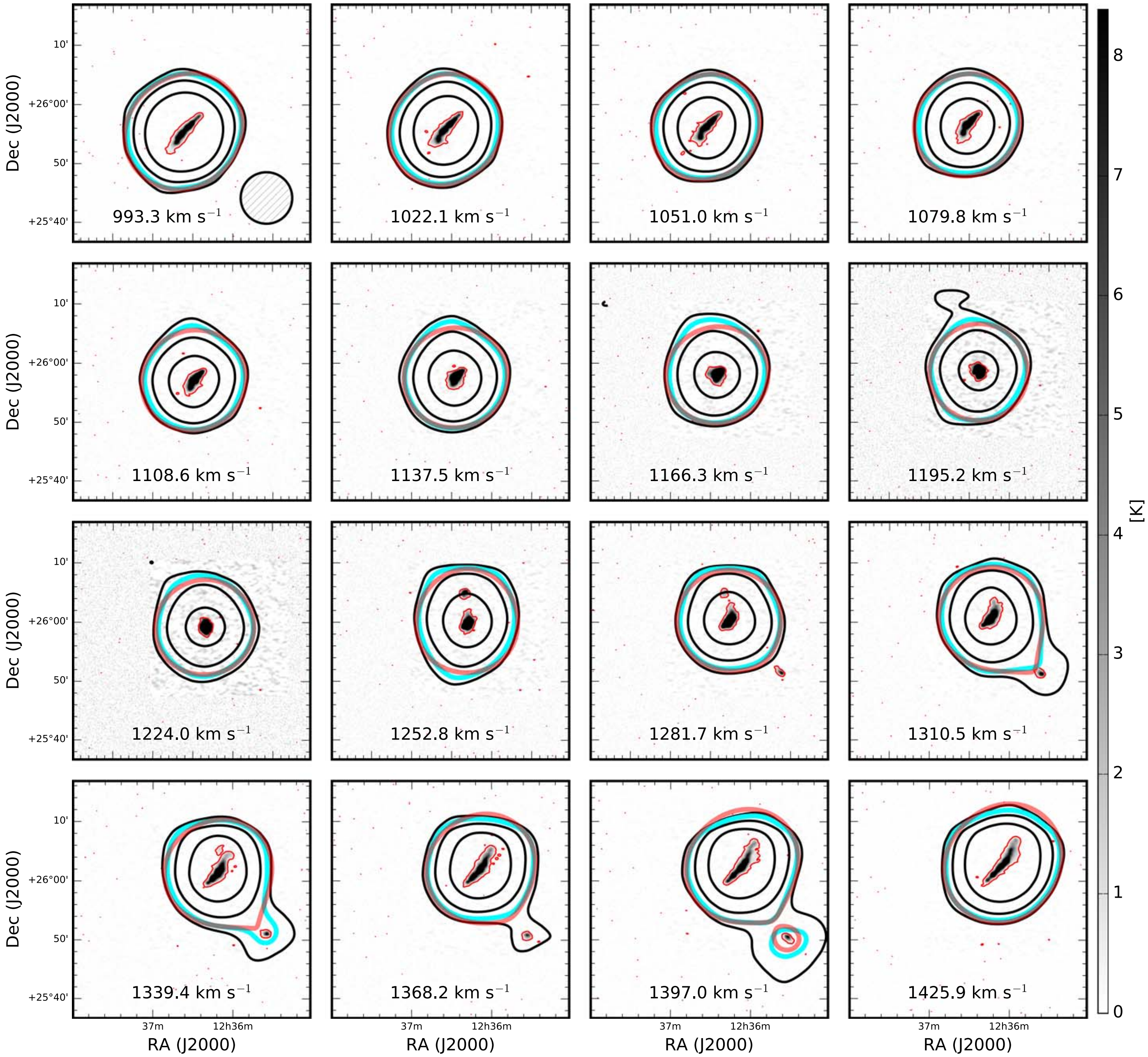

Figure 14. Selected channel maps of the NGC 4565 WSRT data cube with corresponding GBT channel maps superimposed. The GBT data are shown in black and cyan contours at levels of −3 (dashed), 3, 5 (thick cyan), and 25 times 0.01 K, or equivalently a column density level of 1.12×10^{17} cm^{-2} per 4.12 km s^{-1} velocity channel. The grayscale shows the H I emission from the WSRT cube. The thin red line denotes a brightness temperature of 0.54 K, or a column density level at 4.05×10^{18} cm^{-2}, and the thick red line denotes emission at 5.60×10^{17} cm^{-2} (the same level of the cyan contour) in the primary-beam corrected WSRT cube convolved down to the GBT resolution. The GBT beam is shown in the top left panel.

work are at different distances, span a range of physical scales, and are in general inhomogeneous, acute attention to several resolution indicators, which will be discussed in the following discussion, is required to ensure a f_{19} value for a given galaxy is not biased by resolution effects.

The f_{19} values are summarized in Table 3. In general, the f_{19} values derived from the convolved WSRT data are similar to their regridded GBT counterparts. In the cases where the convolved WSRT values are higher, the increase can be attributed to the increased column density sensitivity when the WSRT data (where emission fills the synthesized beam) is convolved to low resolution. In addition to the four sources discussed previously, we also compute f_{19} for three galaxies that have similar GBT data: NGC 2403 (also a HALOGAS source; Fraternali et al. 2001, 2002; de Blok et al. 2014), NGC 2997 (Pisano 2014), and NGC 6946 (with additional deep WSRT data; Boomsma et al. 2008; Pisano 2014).

Our initial small sample size inhibits us from making any significant conclusions about the relations between fraction of diffuse H I and any of the properties that trace simulation predictions. However, investigating the trends within our initial small sample will provide insight on any underlying correlations that may be revealed as we build up our sample and flesh out issues due to resolution effects.

As mentioned previously, it is critical to rule out observational or resolution bias as a source for potential trends.

Table 3
Summary of Derived Properties

Derived Properties	NGC 891	NGC 925	NGC 2403	NGC 2997	NGC 4414	NGC 4565	NGC 6946
GBT H I Mass ($10^9\ M_\odot$)	3.86 ± 0.19	5.79 ± 0.29	3.39 ± 0.37	7.0 ± 1.0	5.43 ± 0.27	7.33 ± 0.37	3.80 ± 0.69
Conv. WSRT H I Mass ($10^9\ M_\odot$)	3.81 ± 0.19	5.54 ± 0.28	⋯	⋯	4.56 ± 0.22	7.46 ± 0.39	⋯
High-res. WSRT H I Mass ($10^9\ M_\odot$)	3.90 ± 0.18	5.57 ± 0.28	⋯	⋯	4.63 ± 0.23	7.55 ± 0.38	⋯
M_* ($10^{10}\ M_\odot$)	0.30 ± 0.10	4.40 ± 0.10	0.39 ± 0.01	8.70 ± 0.10	4.15 ± 0.10	6.15 ± 0.10	0.12 ± 0.01
$M_{\rm bary}$ ($10^{10}\ M_\odot$)	0.82 ± 0.02	5.20 ± 0.10	0.86 ± 0.03	9.71 ± 0.18	4.89 ± 0.10	7.15 ± 0.10	6.29 ± 0.59
Deprojected Physical Area (kpc^2)	603 ± 6	490 ± 6	122 ± 3	726 ± 11	241 ± 24	976 ± 10	416 ± 3
$V_{\rm rot}$[a] (km s^{-1})	212 ± 2	105 ± 2	196 ± 1	145 ± 3	218 ± 6	244	315 ± 12
WSRT f_{19}	0.011 ± 0.001	0.014 ± 0.001	⋯	⋯	0.064 ± 0.004	0.006 ± 0.001	0.004 ± 0.001
GBT f_{19}	0.005 ± 0.001	0.008 ± 0.001	0.005 ± 0.001	0.003 ± 0.001	0.046 ± 0.002	0.008 ± 0.001	0.003 ± 0.001

Note.
[a] Rotation velocity taken from a HYPERLEDA search.

Figure 15(a) plots f_{19} for each source as a function of projected H I angular area computed from the number of pixels above the associated 2σ $N_{\rm H\,I}$ level from Table 2 in the unmasked high-resolution WSRT $N_{\rm H\,I}$ images. Note that in each panel, the blue circles denote f_{19} values derived from convolved WSRT data and the orange inverted triangles represent GBT f_{19} values. The vertical dashed line represents the area of the GBT beam above which extended source structure becomes resolved. While it is encouraging to see all of the projected H I angular area data points fall to the right of the GBT beam area, this is only one indication that our f_{19} parameter is not biased by resolution effects. Because f_{19} is essentially 1 minus the ratio of the integral of the cumulative H I mass distribution taken from bins larger than $Llg_{10}(N_{\rm H\,I}/{\rm cm}^2) = 19.0$ to an integral taken over the full range of $N_{\rm H\,I}$ bins, a better indicator for possible resolution bias is to ensure the data points of the cumulative H I mass distribution for a given source do not trace the simulated unresolved observation (i.e., the GBT beam profile).

In the case of Figure 15(a), the highest f_{19} value is indeed associated with NGC 4414, whose angular area is only a few times that of the GBT beam. Figure 10(b) shows the WRST data cumulative H I mass fraction is consistent with the observation of an unresolved source within the large GBT beam at higher $N_{\rm H\,I}$ bins, while the GBT cumulative H I mass distribution shows only marginal improvement over the simulated unresolved observation. The slight trend between increasing distance and increasing f_{19} values in Figure 15(b) does hint that f_{19} will be influenced by the large GBT beam. The high f_{19} values in both data sets for NGC 4414 reveal how the effects of resolution can bias the calculation of f_{19}. That said, we also see sources with comparable f_{19} values over a large range of projected angular areas whose cumulative H I mass functions do not trace a simulated observation of an unresolved source. Figures 15(a) and (b) thus demonstrate that f_{19} is not generally biased when applied to well-resolved sources.

The physical extent of a diffuse gas reservoir should ideally scale with a diffuse H I mass fraction. Plotting f_{19} as a function of physical projected H I area in Figure 15(c) shows that the highest f_{19} value is associated with the second largest physical extent; however, the high f_{19} value is very likely biased due to the greater distance of the source. On the other hand, the second highest f_{19} value corresponds to the very well-resolved galaxy of NGC 4565, demonstrating the expected scaling. That said, the fact that this particular GBT f_{19} value is the second highest value of the sample by only about a factor of two underscores the lack of a significant diffuse H I around NGC 4565.

A relationship between f_{19} and galaxy properties investigated in simulations (e.g., Kereš et al. 2005, 2009) should give some indication as to whether any newly probed diffuse component could be related to accretion from the IGM. For example, simulations show cold mode accretion is still an available channel for gas accretion around nearby galaxies with relatively low halo masses ($M_{\rm halo} \leqslant 10^{11.4}\ M_\odot$) and in low-density environments. Any trend between excess H I and properties known to be responsible for the presence of excess H I could provide observational evidence, albeit indirect, that the observed excess H I is being accreted directly from the IGM. Figure 15(d) plots f_{19} as a function of galaxy density, or the number of galaxies per Mpc^{-3} (ρ); we estimate ρ by using values derived in Tully (1988). Any correlation between f_{19} and ρ should provide insight into the influence of tidal forces. No obvious trend presents itself here. The absence of a trend in the context of the full sample would be indicative of the relative unimportance of tidal interactions as compared to outflows or accretion to the presence of extraplanar and/or an extended gas reservoir.

Figure 15(e) plots f_{19} as a function of the baryonic mass ($M_{\rm bary}$), where the vertical dashed lines represent the threshold set by the simulations of Kereš et al. (2005), in which cold mode accretion is predicted to be the dominant mechanism of gas accretion. Assuming the dust and molecular gas components to be negligible to the total gas mass, we calculate $M_{\rm bary}$ to be equal to $M_{\rm H\,I} \cdot 1.36 + M_*$, where $M_{\rm H\,I}$ is measured by the GBT. The factor of 1.36 in the leading term corrects for the fraction of neutral He. There is no apparent trend between f_{19} and $M_{\rm bary}$. Additionally, Figure 15(f) presents the relationships between f_{19} and rotational velocity ($V_{\rm rot}$). The dashed line in this plot shows the observational threshold such that galaxies with $V_{\rm rot} \leqslant 125$ km s^{-1} are expected to be gas dominated due to continuous sustained growth (Kannappan 2004; Kannappan et al. 2013). Again, no discernible trend is observed.

The final origin scenario for a large diffuse component in these galaxies is related to outflows due to star formation activity in the disk. The relationship between f_{19} and specific star formation rate (sSFR), which is the SFR per unit stellar mass, is presented in Figure 15(g); f_{19} as a function of the surface density of star formation is shown in Figure 15(h). We derive the surface density of star formation by dividing the SFR

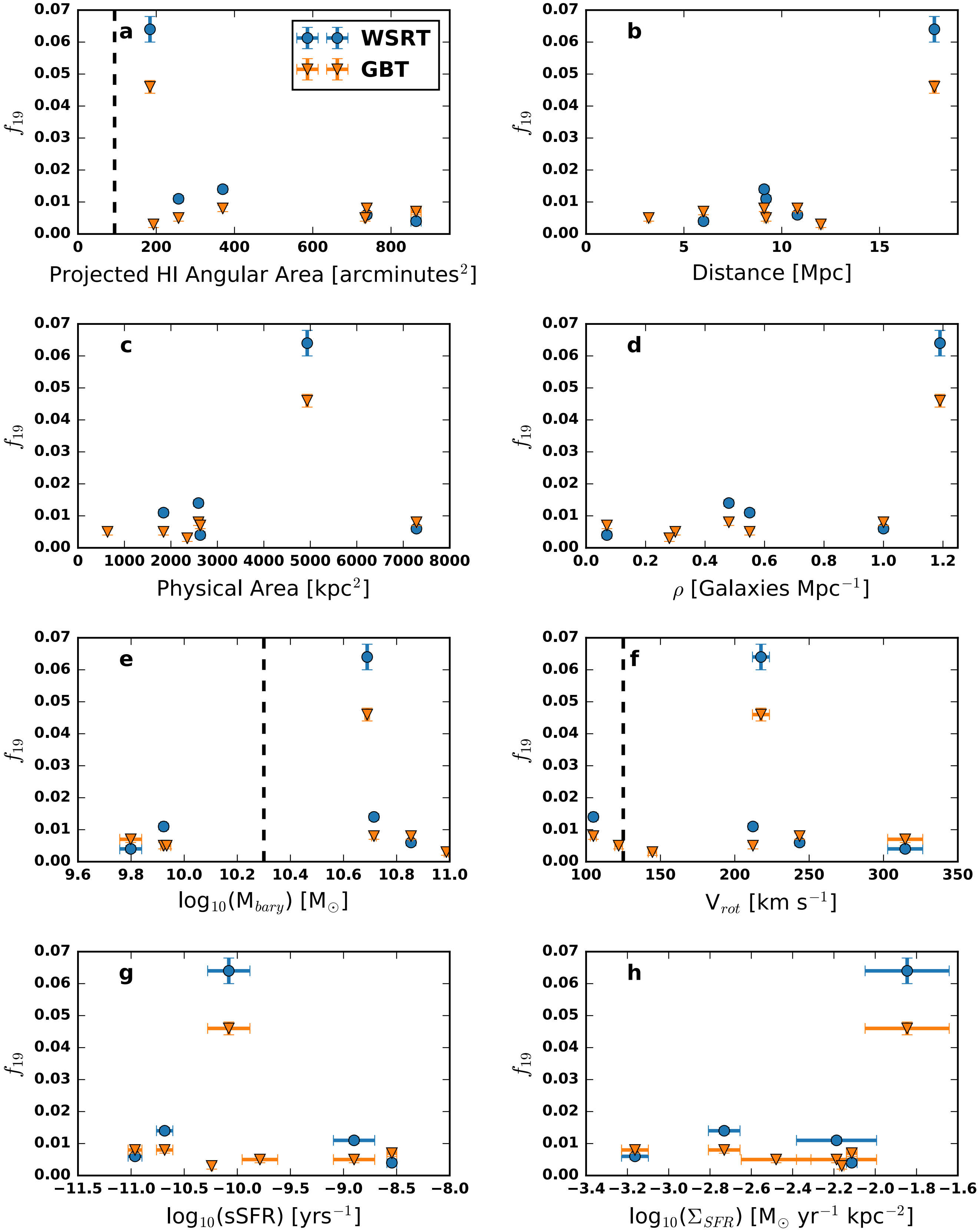

Figure 15. Environmental and intrinsic property relations with excess H I ratio, f_{19}. (a) f_{19} as a function of projected angular area. The vertical dashed line marks the area of the GBT beam (up to the FWHM). (b) f_{19} as a function of distance. (c) f_{19} as a function of projected physical area. (d) f_{19} as a function of galaxy density. ρ is taken from Tully (1988). (e) f_{19} as a function of the source galaxy baryonic mass ($M_{\mathrm{H\,I}} + M_*$). The vertical dashed line corresponds to the baryonic mass threshold from Kereš et al. (2005), below which cold mode accretion is the dominant accretion mechanism. (f) f_{19} as a function of rotational velocity. The vertical dashed line corresponds to the threshold mass at which galaxies should be gas dominated (Kannappan et al. 2013). (g) f_{19} as a function of specific SFR (sSFR). (h) f_{19} as a function of the surface density of star formation (Σ_{SFR}).

by the deprojected physical area. We compute the physical area, assuming each galaxy face-on is roughly circular, and utilize the deprojected and extinction corrected semimajor angular diameter computed from the B-band 25 mag arcsec^{-2} isophote (de Vaucouleurs et al. 1976). Excluding the rightmost data points in Panel (h)—which may, at some level, be biased by resolution—there is no indication of trend between increasing f_{19} with increased star formation activity. A positive correlation suggests more energy per gravitational potential in such galaxies, which points to the possible existence of outflows.

Some, if not most, of the extraplanar gas observed around nearby galaxies must originate from outflows described by galactic fountain (Bregman 1980; Norman & Ikeuchi 1989; Fraternali 2017), and are driven by the injection of momentum and energy into the local interstellar medium from supernovae. In most cases, such outflows are the more feasible origin for diffuse H I in the form of extraplanar gas. Fraternali & Binney (2006, 2008) outline dynamical models that accurately reproduce the general vertical distribution of gas in NGC 891 and NGC 2403 with a necessary energy injection of only <4% of the energy released by supernovae. But while the general distribution is reproduced, the rotational velocity of the model halos is much too high compared to observations. The discrepancy between modeled and observed rotational velocities suggested the acquisition of low-angular momentum gas from the IGM in order to slow the model halos. More recently, however, Marinacci et al. (2010) and Fraternali (2017) show that including the effects of condensation, drag (ram pressure), and radiative cooling in these ballistic models of fountain gas will prevent momentum loss in the cold gas while also increasing the transfer of momentum to intermediate temperature material as opposed to the hot coronal gas. The increase in rotational velocity is therefore mitigated, thus bringing these models into agreement with observational data. By incorporating radiative cooling of the hot coronal gas, it can condense in the wake of fountain clouds, which consequently raises the accretion rate of low-metallicity gas onto the central disk of an embedded galaxy. Specifically, Fraternali (2017) recovers cold gas accretion rates comparable with the the SFR of NGC 891 and NGC 2403.

We end this section by posturing what type of observational constraints between f_{19} and the inherent galaxy properties shown in Figure 15 would indicate the possibility of observing active cold mode accretion. The first necessity would be a f_{19} value from the GBT data that is well above the WSRT and well to the right of the vertical dashed line in Figure 15(a). This would indicate that the WSRT had resolved out significantly extended structure and physical column densities as the emission has filled the large GBT beam. That same large f_{19} GBT data point would then need to be associated with a small ρ to indicate isolation and that tidal interactions are not likely to be the origin of the diffuse environment. We would next need to see the f_{19} value fall below the M_{bary} and V_{rot} thresholds to ensure the galaxy is consistent with the predictions of the cosmological simulations. Finally, the presence of a significant diffuse H I component would need to be associated with a relatively insignificant amount of star formation activity, ruling out the presence of substantial outflows and subsequent condensation from the fountain activity.

The derived properties of these four sources are summarized in Table 3. The columns are (1) source name; (2) H I mass measured in the GBT data; (3) H I mass measured in the convolved WSRT data; (4) H I mass as measured in the high-resolution WSRT data; (5) stellar mass derived from the *WISE* All Sky Image Atlas; (6) baryonic mass; (7) deprojected physical area; (8) rotation velocity from HYPERLEDA; (9) f_{19} measured in the convolved WSRT cube; and (10) f_{19} measured in the GBT cube. The relationships in this section should be considered diagnostic in that we are trying to develop intuition into what trends should exist in galaxies that are actively undergoing cold mode accretion. The low number of sources studied in this work inhibit any conclusions. We will continue to build our statistical sample with future analysis of the HALOGAS, THINGS, and ultimately the MeerKAT HI Observations of Nearby Galactic Objects: Observing Southern Emitters (MHONGOOSE; de Blok et al. 2017) and the Imaging Galaxies Inter-galactic and Nearby Environment (IMAGINE) galaxy samples in order to search for correlations between the presence of a significant diffuse H I environment and the intrinsic galaxy properties that should trace accretion from the IGM in the local universe.

6. Conclusions and Future Work

We presented an initial analysis of deep ($N_{\mathrm{H\,I}} \sim 10^{18}$ cm^{-2}) GBT observations of four sources (NGC 891, NGC 925, NGC 4414, and NGC 4565) out of 24 total sources in the HALOGAS survey. These observations are among the most sensitive H I observations of external galaxies to date. In order to directly compare interferometer and single-dish data, we solve for an optimal smoothing kernel specific to each source and convolve the WST data to GBT angular resolution. Our main conclusions are

1. As we do not find significant spatially extended H I features, we conclude that the WSRT data do an excellent job recovering the diffuse ($18 \leqslant \log_{10}(N_{\mathrm{H\,I}}) \leqslant 19$) H I around these four sources. In the case of NGC 925, we detect about 20% more H I than observations done with the VLA as part of the THINGS survey. The discrepancy is likely due in large part to the increased surface brightness sensitivity of the WSRT data, since the ability to detect extended structure between the two surveys is very similar. The excellent agreement between the global H I profiles, cumulative H I mass as a function of $N_{\mathrm{H\,I}}$, radial mean column density profiles, and radial cumulative flux for the GBT and convolved WSRT data provides additional evidence in support of this conclusion.
2. The cumulative H I mass as a function of H I column density reveals the diffuse H I associated with these galaxies does not change significantly over the range $\log_{10}(N_{\mathrm{H\,I}}/\mathrm{cm}^{-2}) = 18.0$ to $\log_{10}(N_{\mathrm{H\,I}}/\mathrm{cm}^{-2}) = 19.5$. The flat behavior is consistent with predictions from simulations, which show the neutral fraction is around 1% at $\log_{10}(N_{\mathrm{H\,I}}/\mathrm{cm}^{-2}) = 18.0$. Scaling our GBT beam model to the peak column density of the GBT data and repeating our analysis to essentially simulate an unresolved source produces a similarly flat distribution, which suggests the lowest column density bins include some values that trace the extended structure of the GBT beam. That said, there is generally a moderate offset between the data and model cumulative H I mass distributions. The overall agreement between the GBT and WSRT data sets, if extended to the other sources in our survey,

suggests future surveys must probe column densities at the $\sim 10^{17}$ cm^{-2} level to increase the probability of detecting H I associated with cosmic web structure or possibly cold mode accretion.

3. We define a parameter, f_{19}, equal to 1 minus the ratio between the H I mass measured at and above $\log_{10}(N_{\mathrm{H\,I}}) = 19$ and the source's total H I mass. We find that, on average (and excluding data that may suffer from resolution effects), this value is equal to 2%, indicating the diffuse extended disks of these galaxies do not constitute a significant fraction of the overall mass.

One observational method to differentiate between inflow/outflow origins is a measure of metallicity using UV absorption lines (e.g., S II) utilizing the Cosmic Origins Spectrograph on the *Hubble* Space Telescope. If a significant diffuse H I feature is seen around a source as we analyze the full survey, and a fortuitous background quasar along the line of sight, a metallicity of $\sim 0.1\ Z_{\odot}$ would be highly indicative of a CGM origin.

To establish or rule out cold mode accretion as a feasible avenue for nearby galaxies to refuel their gas content, we must continue to analyze galaxies within the HALOGAS sample that satisfy the mass constraints set by simulations, show large diffuse H I mass fractions and low SFRs, and reside in low-density environments. Due to our small sample size, we can only present foundational work to uncover any underlying correlations between large mass fractions of diffuse H I and galaxy properties. Future work will focus on the analysis techniques presented here in order to investigate the origins of these large H I filaments, apply short spacing corrections to the WSRT data, and continue the investigation into role of H I in galaxy evolution.

We thank Richard Prestage and Jay Lockman for insightful discussions on the behavior and geometry of the innermost sidelobes of the GBT. We are also grateful to Filippo Fraternali for his helpful discussions on the caveats of convolving high-resolution data and the interpretation of residual emission. Finally, we thank the anonymous referee for their constructive comments that helped to focus the analysis and conclusions presented in this work. This study was funded by the NSF CAREER grant AST-1149491. The National Radio Astronomy Observatory is a facility of the National Science Foundation operated under cooperative agreement by Associated Universities, Inc. T.H.J. acknowledges financial support from the National Research Foundation (NRF; South Africa).

ORCID iDs

N. M. Pingel https://orcid.org/0000-0001-9504-7386
T. H. Jarrett https://orcid.org/0000-0002-4939-734X
R. J. Rand https://orcid.org/0000-0003-2048-4228
T. Oosterloo https://orcid.org/0000-0002-0616-6971
B. Winkel https://orcid.org/0000-0001-6999-3635

References

Aniano, G., Draine, B. T., Gordon, K. D., & Sandstrom, K. 2011, PASP, 123, 1218
Bekki, K. 2008, MNRAS, 390, L24
Benjamin, R. A. 2002, in ASP Conf. Ser. 276, Seeing Through the Dust: The Detection of HI and the Exploration of the ISM in Galaxies, ed. A. R. Taylor, T. L. Landecker, & A. G. Willis (San Francisco, CA: ASP), 201
Birnboim, Y., & Dekel, A. 2003, MNRAS, 345, 349
Bland-Hawthorn, J., Maloney, P. R., Stephens, A., Zovaro, A., & Popping, A. 2017, ApJ, 849, 51
Boomsma, R., Oosterloo, T. A., Fraternali, F., van der Hulst, J. M., & Sancisi, R. 2008, A&A, 490, 555
Boothroyd, A. I., Blagrave, K., Lockman, F. J., et al. 2011, A&A, 536, A81
Braun, R., & Thilker, D. 2004, in ASP Conf. Ser. 327, Satellites and Tidal Streams, ed. F. Prada, D. M. Delgado, & T. J. Mahoney (San Francisco, CA: ASP), 139
Braun, R., & Walterbos, R. A. M. 1985, A&A, 143, 307
Bregman, J. N. 1980, ApJ, 236, 577
Buat, V., Boissier, S., Burgarella, D., et al. 2008, A&A, 483, 107
Buat, V., Giovannoli, E., Heinis, S., et al. 2011, A&A, 533, A93
Chynoweth, K. M., Langston, G. I., & Holley-Bockelmann, K. 2011, AJ, 141, 9
Cluver, M. E., Jarrett, T. H., Hopkins, A. M., et al. 2014, ApJ, 782, 90
Corbelli, E., Lorenzoni, S., Walterbos, R., Braun, R., & Thilker, D. 2010, A&A, 511, A89
de Blok, W. J. G., Adams, E. A. K., Amram, P., et al. 2017, arXiv:1709.08458
de Blok, W. J. G., Józsa, G. I. G., Patterson, M., et al. 2014, A&A, 566, A80
de Vaucouleurs, G., de Vaucouleurs, A., & Corwin, J. R. 1976, Second Reference Catalogue of Bright Galaxies (Austin, TX: Univ. Texas Press)
Dove, J. B., & Shull, J. M. 1994, ApJ, 423, 196
Driver, S. P., Hill, D. T., Kelvin, L. S., et al. 2011, MNRAS, 413, 971
Driver, S. P., Norberg, P., Baldry, I. K., et al. 2009, A&G, 50, 5.12
Fraternali, F. 2017, in Gas Accretion onto Galaxies Vol. 430, ed. A. Fox & R. Davé (Cham: Springer), 323
Fraternali, F., & Binney, J. J. 2006, MNRAS, 366, 449
Fraternali, F., & Binney, J. J. 2008, MNRAS, 386, 935
Fraternali, F., Marasco, A., Armillotta, L., & Marinacci, F. 2015, MNRAS, 447, L70
Fraternali, F., Oosterloo, T., Sancisi, R., & van Moorsel, G. 2001, ApJL, 562, L47
Fraternali, F., van Moorsel, G., Sancisi, R., & Oosterloo, T. 2002, AJ, 123, 3124
Gil de Paz, A., Boissier, S., Madore, B. F., et al. 2007, ApJS, 173, 185
Gottesman, S. T. 1980, AJ, 85, 824
Heald, G., Józsa, G., Serra, P., et al. 2011, A&A, 526, A118
Heald, G., Józsa, G., Serra, P., et al. 2012, A&A, 544, C1
Jarrett, T. H., Masci, F., Tsai, C. W., et al. 2013, AJ, 145, 6
Jorsater, S., & van Moorsel, G. A. 1995, AJ, 110, 2037
Joung, M. R., Bryan, G. L., & Putman, M. E. 2012, ApJ, 745, 148
Kannappan, S. J. 2004, ApJL, 611, L89
Kannappan, S. J., Stark, D. V., Eckert, K. D., et al. 2013, ApJ, 777, 42
Karachentsev, I. D., & Kaisina, E. I. 2013, AJ, 146, 46
Kauffmann, G., Li, C., & Heckman, T. M. 2010, MNRAS, 409, 491
Kereš, D., Katz, N., Fardal, M., Davé, R., & Weinberg, D. H. 2009, MNRAS, 395, 160
Kereš, D., Katz, N., Weinberg, D. H., & Davé, R. 2005, MNRAS, 363, 2
Lelli, F., Verheijen, M., & Fraternali, F. 2014, MNRAS, 445, 1694
Madau, P., & Dickinson, M. 2014, ARA&A, 52, 415
Maloney, P. 1993, ApJ, 414, 41
Mangum, J. G., Emerson, D. T., & Greisen, E. W. 2007, A&A, 474, 679
Marinacci, F., Fraternali, F., Ciotti, L., & Nipoti, C. 2010, MNRAS, 401, 2451
Marinacci, F., Grand, R. J. J., Pakmor, R., et al. 2017, MNRAS, 466, 3859
Nelson, D., Vogelsberger, M., Genel, S., et al. 2013, MNRAS, 429, 3353
Norman, C. A., & Ikeuchi, S. 1989, ApJ, 345, 372
Noterdaeme, P., Petitjean, P., Carithers, W. C., et al. 2012, A&A, 547, L1
Nuza, S. E., Parisi, F., Scannapieco, C., et al. 2014, MNRAS, 441, 2593
Oosterloo, T., Fraternali, F., & Sancisi, R. 2007, AJ, 134, 1019
Pisano, D. J. 2014, AJ, 147, 48
Pisano, D. J., Wilcots, E. M., & Elmegreen, B. G. 1998, AJ, 115, 975
Popping, A., Davé, R., Braun, R., & Oppenheimer, B. D. 2009, A&A, 504, 15
Putman, M. E., Peek, J. E. G., Muratov, A., et al. 2009, ApJ, 703, 1486
Rahmati, A., Schaye, J., Bower, R. G., et al. 2015, MNRAS, 452, 2034
Rees, M. J., & Ostriker, J. P. 1977, MNRAS, 179, 541
Ribaudo, J., Lehner, N., Howk, J. C., et al. 2011, ApJ, 743, 207
Richter, P., Nuza, S. E., Fox, A. J., et al. 2017, A&A, 607, A48
Rupen, M. P. 1991, AJ, 102, 48
Sancisi, R., & Allen, R. J. 1979, A&A, 74, 73
Sancisi, R., Fraternali, F., Oosterloo, T., & van der Hulst, T. 2008, A&ARv, 15, 189
Sault, R. J., Teuben, P. J., & Wright, M. C. H. 1995, in ASP Conf. Ser. 77, Astronomical Data Analysis Software and Systems IV, ed. R. A. Shaw, H. E. Payne, & J. J. E. Hayes (San Francisco, CA: ASP), 433

Stanimirovic, S. 2002, in ASP Conf. Ser. 278, Single-Dish Radio Astronomy: Techniques and Applications, ed. S. Stanimirovic et al. (San Francisco, CA: ASP), 375

Stocke, J. T., Keeney, B. A., & Danforth, C. W. 2010, PASA, 27, 256

Swaters, R. A., Sancisi, R., & van der Hulst, J. M. 1997, ApJ, 491, 140

Tully, R. B. 1988, Nearby Galaxies Catalog (Cambridge: Cambridge Univ. Press)

van Gorkom, J. 1996, in ASP Conf. Ser. 106, The Minnesota Lectures on Extragalactic Neutral Hydrogen, ed. E. D. Skillman (San Francisco, CA: ASP), 293

Verheijen, M. A. W., & Sancisi, R. 2001, A&A, 370, 765

Wakker, B. P., Savage, B. D., Sembach, K. R., et al. 2003, ApJS, 146, 1

Walter, F., Brinks, E., de Blok, W. J. G., et al. 2008, AJ, 136, 2563

Wolfe, S. A., Lockman, F. J., & Pisano, D. J. 2016, ApJ, 816, 81

Wolfe, S. A., Pisano, D. J., & Lockman, F. J. 2015, GBT Memo Series 289

Wolfe, S. A., Pisano, D. J., Lockman, F. J., McGaugh, S. S., & Shaya, E. J. 2013, Natur, 497, 224

Zhu, Y.-N., Wu, H., Li, H.-N., & Cao, C. 2010, RAA, 10, 329

Zschaechner, L. K., Rand, R. J., Heald, G. H., Gentile, G., & Józsa, G. 2012, ApJ, 760, 37